



**NAVAL
POSTGRADUATE
SCHOOL**

MONTEREY, CALIFORNIA

THESIS

**FIVE-JUNCTION SOLAR CELL OPTIMIZATION USING
SILVACO ATLAS**

by

Raymond J. Kilway II

September 2017

Thesis Advisor:
Second Reader:

Sherif Michael
Matthew Porter

Approved for public release. Distribution is unlimited.

THIS PAGE INTENTIONALLY LEFT BLANK

REPORT DOCUMENTATION PAGE			Form Approved OMB No. 0704-0188
<p>Public reporting burden for this collection of information is estimated to average 1 hour per response, including the time for reviewing instruction, searching existing data sources, gathering and maintaining the data needed, and completing and reviewing the collection of information. Send comments regarding this burden estimate or any other aspect of this collection of information, including suggestions for reducing this burden, to Washington headquarters Services, Directorate for Information Operations and Reports, 1215 Jefferson Davis Highway, Suite 1204, Arlington, VA 22202-4302, and to the Office of Management and Budget, Paperwork Reduction Project (0704-0188) Washington, DC 20503.</p>			
1. AGENCY USE ONLY (Leave blank)	2. REPORT DATE September 2017	3. REPORT TYPE AND DATES COVERED Master's thesis	
4. TITLE AND SUBTITLE FIVE-JUNCTION SOLAR CELL OPTIMIZATION USING SILVACO ATLAS		5. FUNDING NUMBERS	
6. AUTHOR(S) Raymond J. Kilway II			
7. PERFORMING ORGANIZATION NAME(S) AND ADDRESS(ES) Naval Postgraduate School Monterey, CA 93943-5000		8. PERFORMING ORGANIZATION REPORT NUMBER	
9. SPONSORING /MONITORING AGENCY NAME(S) AND ADDRESS(ES) N/A		10. SPONSORING / MONITORING AGENCY REPORT NUMBER	
11. SUPPLEMENTARY NOTES The views expressed in this thesis are those of the author and do not reflect the official policy or position of the Department of Defense or the U.S. Government. IRB number <u>N/A</u> .			
12a. DISTRIBUTION / AVAILABILITY STATEMENT Approved for public release. Distribution is unlimited.		12b. DISTRIBUTION CODE	
<p>13. ABSTRACT (maximum 200 words)</p> <p>Multi-junction solar cells have given rise to compact high-efficiency photovoltaic devices, which offer significant improvements over conventional single-junction solar cell designs. This research uses an existing five-junction solar cell design by Fraunhofer ISE to provide the baseline structure for a simulation model based on published cell characteristics. This structure is then optimized by varying doping concentration and material thickness in each active cell layer in order to increase overall photocurrent generation and maximize efficiency. Optimization of solar cell efficiency is carried out via nearly orthogonal balanced design of experiments methodology. Silvaco ATLAS is utilized to simulate the behavior of the multi-junction solar cells' configurations sampled in the design space. The results of the simulations of points within the sampled design space are loaded into statistical analysis software to construct a stepwise linear regression model to predict the optimum input parameter values to maximize output power and efficiency. The predicted optimum design point is then simulated in the Silvaco ATLAS model. Simulation results are compared to the baseline to analyze improvements such as external quantum efficiency, recombination rate, and current generation. The results following the optimization raised the multi-junction cell output power efficiency from 26.2166% to 37.3682%, while the external quantum efficiencies of the second, third, and fourth junctions were raised 8% to 20%.</p>			
14. SUBJECT TERMS multi-junction, solar cell, Silvaco ATLAS, NOLH, NOB, optimization, simulation, modeling			15. NUMBER OF PAGES 99
			16. PRICE CODE
17. SECURITY CLASSIFICATION OF REPORT Unclassified	18. SECURITY CLASSIFICATION OF THIS PAGE Unclassified	19. SECURITY CLASSIFICATION OF ABSTRACT Unclassified	20. LIMITATION OF ABSTRACT UU

THIS PAGE INTENTIONALLY LEFT BLANK

Approved for public release. Distribution is unlimited.

FIVE-JUNCTION SOLAR CELL OPTIMIZATION USING SILVACO ATLAS

Raymond J. Kilway II
Lieutenant Commander, United States Navy
B.S., University of Notre Dame, 2005

Submitted in partial fulfillment of the
requirements for the degree of

MASTER OF SCIENCE IN ELECTRICAL ENGINEERING

from the

NAVAL POSTGRADUATE SCHOOL
September 2017

Approved by: Sheriff Michael
Thesis Advisor

Matthew Porter Second Reader

R. Clark Robertson
Chair, Department of Electrical and Computer Engineering

THIS PAGE INTENTIONALLY LEFT BLANK

ABSTRACT

Multi-junction solar cells have given rise to compact high-efficiency photovoltaic devices, which offer significant improvements over conventional single-junction solar cell designs. This research uses an existing five-junction solar cell design by Fraunhofer ISE to provide the baseline structure for a simulation model based on published cell characteristics. This structure is then optimized by varying doping concentration and material thickness in each active cell layer in order to increase overall photocurrent generation and maximize efficiency. Optimization of solar cell efficiency is carried out via nearly orthogonal balanced design of experiments methodology. Silvaco ATLAS is utilized to simulate the behavior of the multi-junction solar cells' configurations sampled in the design space. The results of the simulations of points within the sampled design space are loaded into statistical analysis software to construct a stepwise linear regression model to predict the optimum input parameter values to maximize output power and efficiency. The predicted optimum design point is then simulated in the Silvaco ATLAS model. Simulation results are compared to the baseline to analyze improvements such as external quantum efficiency, recombination rate, and current generation. The results following the optimization raised the multi-junction cell output power efficiency from 26.2166% to 37.3682%, while the external quantum efficiencies of the second, third, and fourth junctions were raised 8% to 20%.

THIS PAGE INTENTIONALLY LEFT BLANK

TABLE OF CONTENTS

I.	INTRODUCTION.....	1
	A. PREVIOUS WORK AT NPS.....	1
	B. OBJECTIVE	2
	C. ORGANIZATION	3
II.	BACKGROUND	5
	A. SEMICONDUCTOR BASICS.....	5
	1. Compound Semiconductors and Alloys.....	6
	2. Charge Carrier Transport	7
	3. P-N Junctions	9
	4. Optical Properties of Semiconductors	10
	B. SOLAR CELLS.....	11
	1. Solar Cell Structure	12
	2. Key Solar Cell Parameters and Metrics	14
	3. Multi-junction Solar Cells.....	16
	4. Current Multi-junction Cell Records	18
	C. SOLAR CELL DESIGN OPTIMIZATION.....	21
	1. Genetic Algorithms	21
	2. NOLH/NOB Design of Experiments Optimization.....	23
III.	EXPERIMENTAL DESIGN.....	25
	A. MODEL BASELINE—FRAUNHOFER ISE 5-J CELL	25
	B. MODEL DEVELOPMENT AND BASELINE	28
	1. Model Development Procedure	28
	2. Baseline Cell	37
	C. INPUT FACTOR SELECTION AND OPTIMIZATION USING NOB DOE	39
IV.	EXPERIMENTAL RESULTS.....	43
	A. BASELINE RESULTS	43
	B. OPTIMIZATION ITERATION NO. 1.....	47
	C. OPTIMIZATION ITERATION NO. 2.....	48
	D. OPTIMIZATION ITERATION NO. 3.....	51
	E. OPTIMIZED CELL RESULTS FROM ITERATION NO. 2 MODEL	53
V.	CONCLUSIONS AND FUTURE WORK	61

A.	CONCLUSIONS	61
B.	FUTURE WORK	62
1.	Conduct Optimization with 128-bit Precision and More Design Runs	62
2.	Refractive Index Files	62
3.	Physical Tunnel Junctions.....	62
4.	Material Variance in Design	63
5.	Parallel Processing via a Supercomputer	63
6.	Physical Fabrication of Multi-junction Cell Design	63
7.	Alternative Designs Explored	63
8.	Simulate with Different Air Mass Spectrums	63
APPENDIX A. ATLAS BASELINE INPUT DECK		65
A.	BASELINE SILVACO ATLAS INPUT DECK.....	65
B.	EXAMPLE SILVACO ATLAS CODE FOR FINDING EQE FOR A CELL	71
APPENDIX B. PYTHON SCRIPTS		73
A.	PREPROCESSING SCRIPT TO GENERATE RUN FILES	73
B.	RUN SCRIPT TO EXECUTE SILVACO ATLAS RUNS.....	74
C.	POSTPROCESSING SCRIPT TO EXTRACT OUTPUT POWER	75
LIST OF REFERENCES		77
INITIAL DISTRIBUTION LIST		81

LIST OF FIGURES

Figure 1.	Bandgaps for Conductors, Semiconductors, and Insulators. Source: [1].....	6
Figure 2.	Carrier Diffusion Current (left) and Drift Current (right). Adapted from [1].	7
Figure 3.	P-n Junction Formation. Source: [12].....	10
Figure 4.	Values of k and α for a Material with Bandgap Equating to $0.67 \mu\text{m}$	11
Figure 5.	Spectral Power at Different Air Masses. Source: [12].....	13
Figure 6.	IV Characteristic Curve for a Solar Cell. Source: [2].....	15
Figure 7.	Example EQE for a Three-Junction Cell. Source: [1].	16
Figure 8.	Example Triple Junction Solar Cell. Source: [1].....	18
Figure 9.	Fraunhofer ISE / Soitec Concentrator 4-J Solar Cell Record Holder IV Characteristic. Source: [17].	19
Figure 10.	Fraunhofer ISE / Soitec Concentrator 4-J Solar Cell Record Holder EQE. Source: [17].	19
Figure 11.	Boeing-Spectrolab 5-J Solar Cell Record Holder IV Characteristic. Source: [18].....	20
Figure 12.	Boeing-Spectrolab 5-J Solar Cell Record Holder EQE. Source: [18].	21
Figure 13.	Example Chromosome Utilized by Bates. Source: [2].....	22
Figure 14.	Fraunhofer ISE 5-J Solar Cell #1872 with Improved Radiation Hardness. Source: [9].....	25
Figure 15.	5-J Cell EQE before and after 1 MeV Irradiation. Source: [6].....	26
Figure 16.	IV Characteristic of Fraunhofer ISE 5-J Solar Cell Used for Modeling. Source: [9].....	27
Figure 17.	Baseline Multi-junction Solar Cell Configuration. Adapted from [1], [9].....	38
Figure 18.	Spreadsheet Snippet from Vieira's NOB DoE Implementation. Source: [28].....	39

Figure 19.	Baseline Cell IV Characteristic.....	43
Figure 20.	Baseline Cell Power versus Voltage	44
Figure 21.	Baseline Cell EQE	45
Figure 22.	Electric Fields in Baseline Cell.....	46
Figure 23.	Baseline Cell Area of Highest Recombination Rate.....	47
Figure 24.	Iteration No. 1 Output Power Distributions with Outliers (left) and without Outliers (right)	48
Figure 25.	Iteration No. 2 Output Power Distributions with and without Outliers....	49
Figure 26.	Using the Profiler for Predicting Optimum Input Factor Values.....	51
Figure 27.	Iteration No. 3 Output Power Distributions with and without Outliers	52
Figure 28.	Iteration No. 3 Profiler with Widening Confidence Intervals.....	53
Figure 29.	Optimized 5-J Cell Based on Iteration No. 2 Model	54
Figure 30.	Optimized Cell IV Characteristic Curve.....	55
Figure 31.	Optimized Cell Power versus Voltage.....	56
Figure 32.	Optimized Cell EQE	57
Figure 33.	Electric Fields in Optimized Cell.....	58
Figure 34.	Optimized Cell Area of Highest Recombination Rate.....	59

LIST OF TABLES

Table 1.	Material Parameters Used in Input Deck	31
Table 2.	Material Parameters Used in Input Deck Continued.	31
Table 3.	Silvaco ATLAS Baseline Results	44
Table 4.	Iteration No. 2 Most Important Design Parameters and Relationships	50
Table 5.	Iteration No. 2 Linear Regression Model Fit.....	50
Table 6.	Iteration No. 3 Linear Regression Model Fit.....	53
Table 7.	Silvaco ATLAS Optimized Cell Results and Comparison	55

THIS PAGE INTENTIONALLY LEFT BLANK

LIST OF ACRONYMS AND ABBREVIATIONS

4-J/5-J	four-junction / five-junction
AlGaAs	aluminum gallium arsenide
AlGaInAs	aluminum gallium indium arsenide
AlGaInP	aluminum gallium indium phosphide
AM	air mass
AM0	air mass zero
BSF	back-surface field
DoE	design of experiments
E_c	conduction band energy level
E_g	bandgap energy level
EHP	electron-hole pair
EQE	external quantum efficiency
E_v	valence band energy level
FF	fill factor
GaAs	gallium arsenide
Ge	germanium
GaInAs	gallium indium arsenide
GaInAsP	gallium indium arsenide phosphide
GaInP	gallium indium phosphide
h	Planck's constant (6.626E-34 J-s)
MOVPE	metalorganic vapor phase epitaxy
MUN/MUP	mobility of electrons/holes in Silvaco ATLAS
k	Boltzmann constant (1.381E-23 J-K ⁻¹)
n	electron carrier concentration
n-type	doped semiconductor with electrons as majority carriers
NC	density of states for holes
NOB	nearly orthogonal balanced
NOLH	nearly orthogonal Latin hypercubing
NPS	Naval Postgraduate School
NV	density of states for electrons

p	hole carrier concentration
p-type	doped semiconductor with holes as majority carriers
q	charge of an electron (1.602E-19 C)
Si	silicon

ACKNOWLEDGMENTS

I would like to thank Professor Sherif Michael for his guidance and direction on solar cells and current technologies. I would also like to thank Matthew Porter and Joseph O'Connor for the immeasurable help in learning the basic and advanced techniques of Silvaco ATLAS simulation. Finally, I would like to thank my wife, Katie, for her patience and support while I worked for months on end trying to achieve expected simulation results. I would not have been able to complete this research without the help of these people.

THIS PAGE INTENTIONALLY LEFT BLANK

I. INTRODUCTION

Solar cell technology has evolved dramatically since its birth in the mid-19th century. As society looks to lessen its carbon footprint, solar cells have become an increasingly cost-effective and efficient option to provide green energy in both consumer arenas as well as defense-related matters. Modern defense applications of solar cells include (but are not limited to) installation consumers looking to offset their energy costs, forward operating bases needing reliable mobile power solutions, and the continuing need to provide compact, efficient solar energy sources for military satellites. The latter application traditionally employs multi-junction solar cells, which are more expensive but vastly more efficient and power dense than those used for terrestrial applications, presenting an attractive option when designing satellite power systems. While multi-junction cells in general have outperformed single cell designs, output power efficiency of multi-junction cells continues to improve. The overall efficiency of multi-junction solar cells is a complicated function of the materials used to fabricate the cells, layer thickness, layer doping concentration, and secondary parasitic aspects such as tunnel junction efficiency.

Due to the actual fabrication of multi-junction solar cells being a costly endeavor, it is advantageous (and necessary) to optimize cell performance via simulation prior to fabrication. Physics-based environments for the simulation of semiconductor devices such as Silvaco ATLAS provides a tool to explore the solar cell design space to maximize solar cell efficiency prior to device fabrication.

A. PREVIOUS WORK AT NPS

Work carried out previously at the Naval Postgraduate School (NPS) has successfully demonstrated the effectiveness of Silvaco ATLAS for the optimization of solar cell designs. In 2002, Michalopoulos developed and simulated single, double, and triple junction cells at a time when little research had been performed and compared to Silvaco ATLAS simulation results [1]. In 2004, Bates expanded on Michalopoulos' work by optimizing the designs using a genetic algorithm approach [2]. In 2008, Tsutagawa expanded on the previous work

and sought to optimize a Japanese cell design using a germanium (Ge) layer and other optimization techniques [3]. In 2013 and 2006, Tsutagawa and Utsler, respectively, applied genetic algorithm optimization to single and dual-junction designs and modeled the designs in Silvaco ATLAS with newer modeling techniques [4], [5]. In 2017, O'Connor designed and simulated solar cells in Silvaco ATLAS utilizing a back-surface contact approach and compared the results with industry photovoltaics [6]. Additionally, in 2017, Püschel utilized Tsutagawa's dual-junction design and applied nearly orthogonal Latin hypercubing (NOLH) optimization to achieve better efficiencies [7].

B. OBJECTIVE

The goal of this thesis research was to take an established five-junction solar cell design and optimize its design via an efficient, readily available method. The five-junction design chosen was based off of a multi-junction solar cell designed at the Fraunhofer Institute for Solar Energy Systems (ISE) by Dimroth et al. in 2003 and 2006 [8], [9]. The five junction cell fabricated in 2006 utilized aluminum gallium indium phosphide (AlGaInP), gallium indium phosphide (GaInP), aluminum gallium indium arsenide (AlGaInAs), gallium indium arsenide (GaInAs), and Ge to form the active junctions. The Fraunhofer ISE multi-junction cell was designed to be radiation-resistant and exhibited an experimental efficiency of 20-24% [9]. Limitations in the design related to losses in the tunnel junctions, inefficient peak tunnel current densities, and top cell poor performance coupled with low shunt resistance [9].

For this work, the Fraunhofer ISE five-junction cell design served as the baseline from which to begin optimization via simulation within Silvaco ATLAS. All previous research at NPS in Silvaco ATLAS has dealt with at most three-junction cells, but the lessons learned and coding methods were utilized in developing a simulation of the five-junction cell studied in this work. Challenges included selection of appropriate refractive index values for the materials contained within the design, proper material selection for the layers not specified in the Fraunhofer ISE multi-junction cell, and deriving or locating parameter values for the material definitions. Tunnel junctions were simulated via a metal junction isolated from ground via an external high-impedance resistor.

The optimization method applied in this thesis to the baseline cell was NOLH / nearly orthogonal balanced (NOB) design of experiments (DoE). This statistical method uses simulation input variables and bounds and generates a number of “runs” with randomized variations of the parameters, specifically layer thickness and doping concentration in each cell. Although the bottom cell Ge layer’s doping concentration was varied in the optimization, the overall layer thickness of ~150 microns was maintained constant to best simulate real-world solar cell designs with thick bottom substrates. These runs were executed via a Python script that calls instances of Silvaco ATLAS in series for each of the generated runs. Finally, simulation space results from the Silvaco ATLAS runs were analyzed via the statistical processing suite JMP by fitting the data to a linear regression model to determine the most influential factors and values to achieve the highest cell efficiency. The optimal parameters predicted by JMP were re-run in the developed Silvaco ATLAS model to compare the predicted efficiency with the simulated results. An analysis of electric fields and recombination rates in the multi-junction cell were compared between the baseline cell and the optimized cell to determine the reasons behind changes in output power efficiency.

C. ORGANIZATION

This thesis is organized as follows. Background information concerning semiconductors, solar cell basics, and optimization techniques with regard to this thesis are discussed in Chapter II. Experimental design concerning the model cell, Silvaco ATLAS modeling, and input factor selection for optimization are discussed in Chapter III. Model and optimization results are addressed in Chapter IV. Overall conclusions and future work recommendations regarding the research are covered in Chapter V.

THIS PAGE INTENTIONALLY LEFT BLANK

II. BACKGROUND

Basic information on semiconductors and solar cells as they pertain to this thesis, including a brief history of solar cell technology, is discussed in the opening chapter. Brief discussion on solar cell optimization techniques closes the chapter.

A. SEMICONDUCTOR BASICS

The bandgap of a semiconductor is defined as the energy difference separating the conduction and valence energy bands of a semiconductor material. When valence electrons receive sufficient energy to overcome the bandgap, a conduction band electron is created, leaving behind a positively charged “hole” in the valence band. The bandgap E_g contains no allowed energy levels for electrons to occupy and is known as the “forbidden band” [10]. How big the bandgap is between the bands is determined by the material. Bandgap differences between conductors, semiconductors, and insulators are shown in Figure 1. For conductors, the conduction and valence bands overlap, leading to no bandgap. Electrons are free to move immediately at any temperature above absolute zero, as they do not require any energy to be freed from the valence band. Semiconductors at 0 K behave the same as insulators by exhibiting a filled valence band and an empty conduction band separated by a bandgap [10]. The difference lies in the size of the bandgap, with semiconductors exhibiting relatively small bandgaps compared to insulator’s large bandgaps. Conductivity within the material increases exponentially with temperature, as valence electrons must gain an energy of the bandgap or greater to conduct charge.

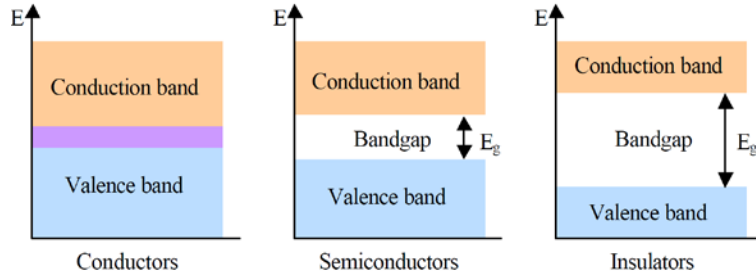


Figure 1. Bandgaps for Conductors, Semiconductors, and Insulators.

Source: [1].

Semiconductors at room temperature have a large number of electrons excited across the bandgap into the conduction band due solely to temperature [10]. Optical excitation of the material also drastically increases the number of free electrons available. In intrinsic semiconductors, the number of holes is equal to the number of electrons, and both are collectively known as charge carriers. This can be changed by doping the material with impurities to designate one carrier as the majority and the other as the minority.

Adding substitutional impurities known as dopants to semiconductors changes the properties according to the amount of the impurity introduced. Dopants serve to add charge carriers based upon their valence. Doped semiconductors are known as n-type when the majority charge carrier is electrons and p-type when the majority carrier is holes [11].

1. Compound Semiconductors and Alloys

Aside from elemental semiconductors, elements can ionically and covalently bond in order to form compound semiconductors. Compound semiconductors of the same family can be alloyed with varying mole fractions to develop materials with properties intermediate between the constituent components of the alloy. Examples of ternary and quaternary alloys within the III-V material family are GaInP and AlGaInAs. Representation of the mole fractions commonly comes in the form of subscripts next to the various elements [10]. An example using a quaternary alloy researched in this thesis is $(Al_{0.3}Ga_{0.7})_{0.5}In_{0.5}P$. In this case, the mole fractions both within and without the

parentheses describe the Group-III sublattice of the compound composed of aluminum, gallium, and indium.

2. Charge Carrier Transport

Under most conditions in semiconducting devices greater than 100 nm in size, the flow of charge carriers occurs by either drift or diffusion, illustrated in Figure 2. Diffusion involves the spatial variation, or gradient, between n and p in a material bringing about net motion of carriers from areas of high carrier concentration to areas of low carrier concentration. Net charge flow occurs by random thermal motion and scattering due to the gradient [10]. Drift occurs due to the force applied to the charge carrier when an electric field is applied to a material. Holes drift in the direction of the applied field, while electrons flow in the opposite direction.

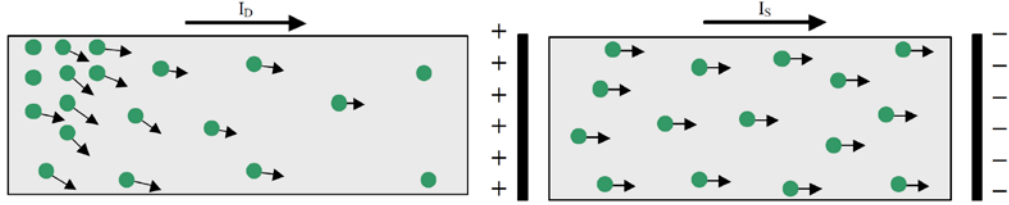


Figure 2. Carrier Diffusion Current (left) and Drift Current (right).
Adapted from [1].

In three dimensions, the steady-state hole current density $J_p(\vec{x})$ and electron current density $J_n(\vec{x})$ in the drift-diffusion model are given by [12]

$$J_p(\vec{x}) = J_{p-drift}(\vec{x}) + J_{p-diff}(\vec{x}) = q\mu_p p(\vec{x})\vec{E}(\vec{x}) - qD_p \vec{\nabla}p(\vec{x}) \quad (1)$$

and

$$J_n(\vec{x}) = J_{n-drift}(\vec{x}) + J_{n-diff}(\vec{x}) = q\mu_n n(\vec{x})\vec{E}(\vec{x}) + qD_n \vec{\nabla}n(\vec{x}) \quad (2)$$

where q is the charge of an electron, μ_p and μ_n are the hole and electron mobilities, respectively, $p(\vec{x})$ and $n(\vec{x})$ are the position-related concentrations of holes and electrons, respectively, $\vec{E}(\vec{x})$ is the position-related electric field, D_p and D_n are the carrier diffusion coefficients, and $\vec{\nabla}p(\vec{x})$ and $\vec{\nabla}n(\vec{x})$ are the gradients of carrier

concentration with respect to position. The sections containing mobility describe the drift component of the current densities, and the sections containing diffusion coefficients describe the diffusion component of the current densities. The total current density $J(x)$ in a material is the sum of the hole and electron contributions given by [12]

$$J(\vec{x}) = J_p(\vec{x}) + J_n(\vec{x}). \quad (3)$$

The total current flowing in a material may be due primarily to either the electrons or holes and depends on what doping level the material has as well as the relative electric field and carrier gradient magnitudes.

The mobilities of the electrons and the holes describe the ability to which an electron or hole has to drift in the material. The mobilities take into account the carrier collisions with impurities imbedded in the material and within the lattice structure as well as collisions with lattice vibrations known as phonons [10]. The carrier mobility is dependent on both temperature and doping concentration and is an important property in describing the behavior of semiconductor materials.

The presence of charged carriers such as electrons and holes as well as ionizing impurities directly affects the electric field. The governing relationship between charge and electric field is the Poisson equation [10]. The Poisson equation is given by [12]

$$\nabla^2 \psi_i = \nabla^2 \left(-\frac{\vec{E}_i(\vec{x})}{q} \right) = \frac{q[n(\vec{x}) - p(\vec{x}) + N_A - N_D]}{\epsilon_s} \quad (4)$$

where $\vec{E}_i(\vec{x})$ is the intrinsic band energy, N_A is the acceptor concentration, N_D is the donor concentration, and ϵ_s is the permittivity of the semiconductor.

Transport of charge carriers in semiconductors is fully described by coupling the drift diffusion current equations and the Poisson electrostatic equation with the principle that electron and hole numbers must be conserved. The continuity equations are the statement of this local conservation of particle number, taking into account the fact that electrons and holes can be removed by processes such as carrier generation and recombination, and are given by [12]:

$$\frac{\partial n}{\partial t} = G_n - U_n + \frac{1}{q} \nabla \cdot J_n \quad (5)$$

and

$$\frac{\partial p}{\partial t} = G_p - U_p - \frac{1}{q} \nabla \cdot J_p \quad (6)$$

where G_n and G_p are, respectively, the electron and hole generation rates in $(\text{cm}^{-3}\text{s}^{-1})$ and U_n and U_p are, respectively, the electron and hole recombination rates $(\text{cm}^{-3}\text{s}^{-1})$.

The current density equations, the Poisson equation, and the continuity equations together describe the governing semiconductor physics equations. Device physics simulation programs such as the Silvaco ATLAS simulation environment described in Chapter III solve these equations.

3. P-N Junctions

A p-n junction is a two-terminal device formed by an abrupt junction where an n-type material with donor impurities meets a p-type material with acceptor impurities [12]. The physics of p-n junctions are central to understanding the operation of solar cells. A simple depiction of the formation of a p-n junction is shown in Figure 3 [12]. A gradient is created upon junction formation where the high concentration of holes in the p-side diffuse toward the n-side, and the electrons diffuse in the opposite way due to the gradient [11]. A depletion region is formed from the ionized dopants left behind in the formation of the junction. An internal electric field is generated which counteracts the diffusing carriers [11]. The holes continue to drift toward the electric field, and electrons away from the electric field, until an equilibrium state is reached where the diffusion matches the drift. The width of the depletion region depends on material doping on either side of the p-n junction. The key aspect of p-n junctions which is central to solar cells is the formation of a static electric field within the depletion region of the junction.

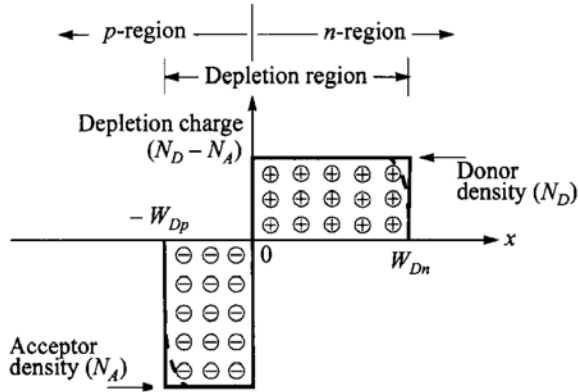


Figure 3. P-n Junction Formation. Source: [12].

4. Optical Properties of Semiconductors

The optical properties of semiconductors are determined by the electronic band structure of the material [12]. Carrier interaction with photons occurs due to the underlying electronic structure of a material in question. Because of this fact, semiconductors do not absorb photons with energy below the bandgap energy of the material. The behavior of optical absorption above the bandgap energy is an involved function of the energy-dispersion relationship.

The refractive index of a solar cell describes the propagation of light through the material. The refractive index is a complex number that both describes the propagation and absorption of light and is given by [12]

$$\bar{n} = n - jk \quad (7)$$

where n represents the real part of the refractive index determined by the dielectric properties of the material and k is the imaginary part referred to as the extinction coefficient, which is related to the ability of the material to absorb light at a given frequency. The refractive index is highly dependent upon light frequency and contains all information needed to describe light propagation in a material. Another more directly measurable optical property is the absorption coefficient. The absorption coefficient α is a measure of the depth of penetration of a photon into a solid and is given by [12]

$$\alpha = \frac{4\pi k}{\lambda}. \quad (8)$$

The extinction coefficient and the absorption coefficient by extension are central to choosing materials useful for solar cell construction. Good solar cell materials must have high absorption at optical wavelengths at which the solar spectrum is prominent. The values for α and k are zero at wavelengths greater than the wavelength equating to the bandgap energy. The extinction and absorption coefficients over a set of wavelengths for a material with a bandgap equating to 0.67 μm are shown in Figure 4.

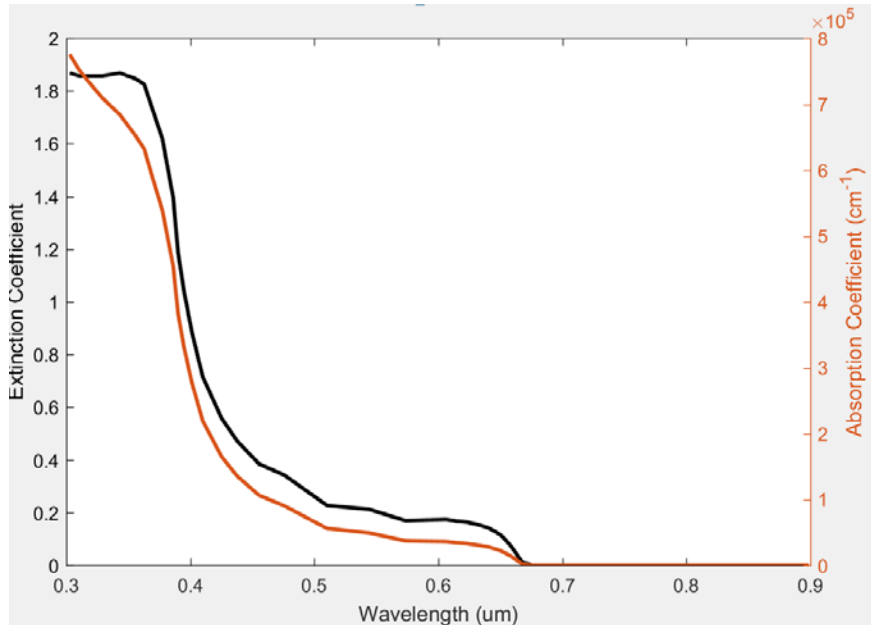


Figure 4. Values of k and α for a Material with Bandgap Equating to 0.67 μm

B. SOLAR CELLS

French physicist Edmond Becquerel first observed the photovoltaic effect, the generation of current or voltage via optical excitation, in 1839 [13]. He built a rudimentary solar cell using an electrochemical cell composed of silver chloride immersed in an acidic solution with electrodes attached to capture the voltage and current [13]. Throughout the latter part of the 19th century, numerous scientists experimented with the photovoltaic effect and rudimentary solar cell technology. The early 20th

century brought about uses of semiconductor junctions in solar cells and the understanding of the quantum basis of solar cells [14]. In the same time period, a method called the Czochralski process was developed that involved the growth of high-purity single crystals of semiconductors and other metals [10]. The process was later used to create large ingots of Si or Ge that could be processed to form wafers used for electronic applications. Silicon p-n junction photocell conversion of solar energy into electrical power was explored in the early 1950s [15]. The theoretical limit of single-junction solar cells, known as the Shockley-Queisser limit, was explored by William Shockley and Hans-Joachim Queisser in 1961 [16]. The calculation determined that using a single p-n junction with bandgap material between 1.3 and 1.4 eV with air mass (AM) 1.5 spectrum light illumination, the maximum output power efficiency achieved could be about a third of the incident light power density converted to useful power output [16]. Multi-junction solar cells were experimented with and developed later in the 20th century to improve upon the Shockley-Queisser limit through the use of materials with high light absorption over a greater fraction of the solar spectrum. Use of multi-junction cells historically has been more cost-prohibitive compared to single-junction alternatives due to the materials chosen for the multi-junction solar cells and the structure of the system itself. Traditionally, this has led to their use in specialized applications only.

1. Solar Cell Structure

Solar cells are illuminated p-n junctions that are designed to take photonic energy from the sun and convert it into usable electrical energy. Photons with energy greater than the bandgap of the cell material contribute to the cell's power output, and excess energy over the bandgap comes off as heat [12]. High performance solar cells have a wide spectral response over the solar spectrum of interest. In this thesis research, we are concerned with the solar spectrum in the near-earth region of the atmosphere. The intensity of the solar spectrum from the sun measured outside the Earth's atmosphere is approximately $1,353 \text{ W/m}^2$ and is referred to as the air mass zero (AM0) spectrum [12]. The AM0 spectrum is presented in Figure 5 along with spectral data for the solar intensity at varying air mass.

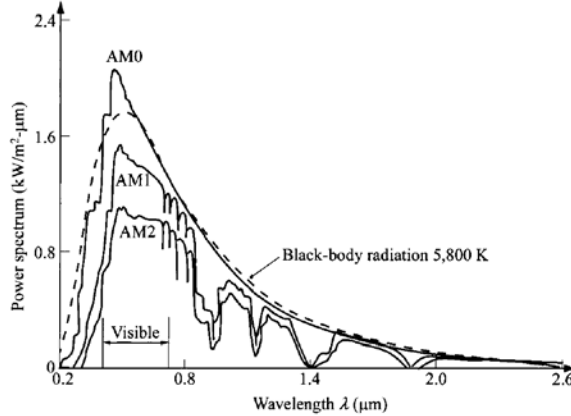


Figure 5. Spectral Power at Different Air Masses. Source: [12].

Photons entering the cell interact within the p-n junction to generate electron-hole pairs (EHPs). The spectral energy of a photon can be related to an associated wavelength by Planck's law. The relationship between the photon energy E in eV and the photon wavelength (λ) in μm is given by [10]

$$E = \frac{hc}{\lambda} = \frac{1.24}{\lambda} \quad (9)$$

with h being Planck's constant in joule-seconds, c being the speed of light in meters per second, and 1.24 being hc converted to eV- μm . If the energy of a photon is greater than the material bandgap, the photon is absorbed into the structure. In direct bandgap semiconductors such as those explored in this thesis, valence electrons are directly excited into the conduction band by photons versus the electron having to pass through an intermediate state [10]. For this reason, direct band materials are preferred for solar applications.

During illumination of the p-n junction, carrier concentration increases. The electric field in the junction sweeps the carriers across the junction, adding to the current. When a short is placed across the junction, only the internal electric field remains present, allowing the measurement of the short circuit current J_{sc} [6]. When no short or external circuit is present across the p-n junction, the built-in field must increase to achieve

equilibrium due to the diffusion current, allowing the measurement of the open circuit voltage V_{oc} [6].

The solar cells explored in this thesis have five parts: a window, an emitter, a base, a back surface field (BSF), and a buffer. The working portion of the solar cell is an n-type emitter on a p-type base. This is the main photoactive p-n junction of the cell with the base making up the bulk of the cell structure and is the central area of carrier photogeneration. The window is used to prevent surface recombination of holes and electrons that decrease output power efficiency by removing current-contributing carriers. The BSF works to increase carriers available for contribution to the photocurrent by directing minority carriers that diffuse away from the junction back toward the junction. Lastly, the buffer at the bottom of the cell acts to negate any electric field forming between the cell and the connecting tunnel junction or substrate that prevent carrier flow.

2. Key Solar Cell Parameters and Metrics

Parameters critical to evaluating the performance of a given solar cell are the short circuit current density J_{sc} , open circuit voltage V_{oc} , maximum power P_{max} , power density, fill factor (FF), and efficiency η . When the p-n junction in a solar cell is short-circuited, all of the current is due to the incident light's intensity and wavelength with no dependence on voltage potential across the junction [11]. The magnitude of this current can be expressed as I_{sc} and is the maximum current the cell can achieve. The short circuit current density J_{sc} is I_{sc} over a given area and is given in mA/cm² in this thesis. Open-circuit conditions for a solar cell leads to a voltage that represents the maximum voltage applied through the cell with no current. The occurrence is due to a built-in field for the p-n junction separating holes to the p side and electrons to the n side and a potential building up between the two sides [11]. The open circuit voltage V_{oc} is the voltage that develops across the device in order to retard current flow.

The maximum power point P_{max} is found by observing the current-voltage (IV) characteristic curve of a solar cell from starting from J_{sc} to V_{oc} . A typical IV curve is shown in Figure 6 with J_{sc} corresponding to the negative of the cell photocurrent. Points along the curve correspond with the increasing voltage due to increasing load resistance.

The power P_{max} corresponds to the knee in the curve with the product of current and voltage leading to the maximum power. The maximum power density is P_{max} over a given area and is given in mW/cm² in this thesis.

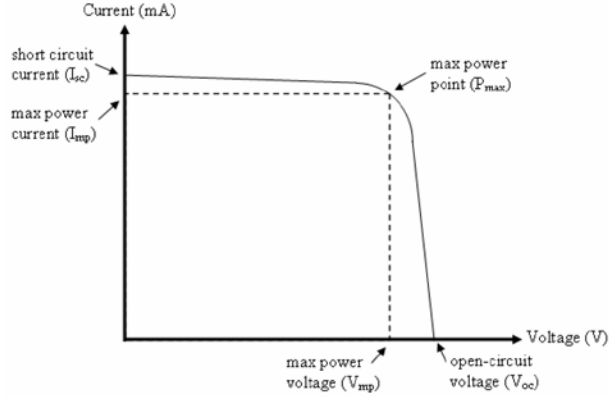


Figure 6. IV Characteristic Curve for a Solar Cell. Source: [2].

The fill factor FF is a measure of the quality of a cell and describes the sharpness of the IV curve [12]. The quality is affected by the shunt resistances present in the cell with a higher fill factor equating to higher shunt resistances in the different material layers. Lower shunt resistances lead to higher power losses and are displayed in the IV characteristic curve as a depressed maximum power point relative to the short circuit condition. The fill factor is given by [12]

$$FF = \frac{I_{mp}V_{mp}}{I_{sc}V_{oc}} = \frac{P_{max}}{I_{sc}V_{oc}} \quad (10)$$

where I_{mp} and V_{mp} correspond to the coordinates of P_{max} . The efficiency η of a solar cell is given by [12]

$$\eta = \frac{P_{max}}{P_{in}} \quad (11)$$

where P_{max} is the maximum output power of the cell and P_{in} is the input power from the light spectrum. The input power is 1,353 W/m² in this thesis.

External quantum efficiency (EQE) is the ratio of carriers collected to the number of photons shining externally on the cell. It is a measure of the utilization of the photons shining on a photovoltaic device and is a function of optical wavelength. The EQE percentage is a measure of the spectral response of a solar cell and can give information regarding the performance of each individual subcell within a multi-junction cell design. EQE measurements form one of the most important solar cell experimental measurements that can be used to explore solar cell performance. Important factors that are revealed by the EQE can be used to improve and further optimize solar cell design. An example EQE spectrum for a three-junction cell with cell junctions of GaInP, GaAs, and Ge, respectively, is shown in Figure 7.

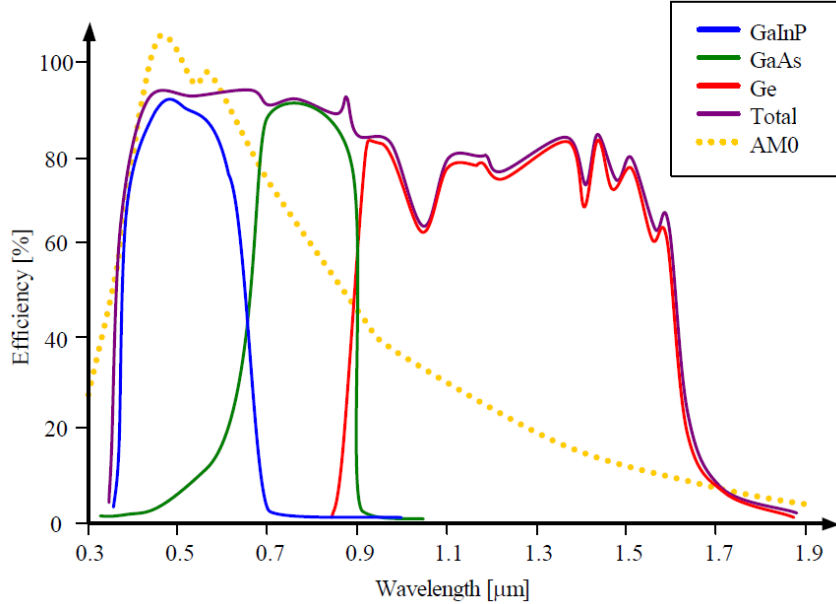


Figure 7. Example EQE for a Three-Junction Cell. Source: [1].

3. Multi-junction Solar Cells

To capture the greatest percentage of wavelengths for a given solar spectrum, multi-junction solar cells are utilized with materials of different bandgaps in order to increase overall cell efficiency. The efficiency gain occurs by stacking cell junctions with lower bandgaps below higher bandgap cell junctions. This allows utilization of a larger

fraction of the incoming solar spectrum that then contributes to overall cell output. These photons were previously not able to interact in the higher bandgap material but can in the lower bandgap material. The overall I_{sc} is limited to the cell with the lowest I_{sc} , while the overall V_{oc} is additive for each cell junction added. The thickness of the overall multi-junction cell, material selection, and doping concentrations determine how much the spectrum is captured and utilized for EHP generation. Past the optimal point for the three parameters described, efficiency losses due to the series resistance come into effect as photons are no longer being generated and thicker layers only serve to increase resistive power loss. Typically, multi-junction solar cells have higher efficiency compared to their single junction counterparts, but the higher efficiency comes with an increased cost of fabrication. For this reason, multi-junction solar cells are typically used in space applications where overall cell development cost is not budget-limited.

An example three-junction cell that was examined by Michalopoulos is shown in Figure 8 [1]. Tunnel junctions act to connect the different cell junctions together without creating electric fields that distort the carrier flow. Tunnel junctions use heavily doped p-n junctions to create low-resistance connections between the active cell layers. Carriers in such junctions quantum-mechanically tunnel between the p and n-sides of the layers, ideally ensuring low junction resistance. High peak tunneling current is key to ensuring optimum cell performance. In working solar cells, high absorption and reflection losses occur in the tunnel junctions that degrade cell performance, and countering this with higher bandgap tunnel junctions leads to larger voltage drops across the junctions [9]. Mechanical stacking of cells prevents these losses but adds to the overall multi-junction cell weight and volume, thus making the method non-ideal for space applications where both parameters are critical.

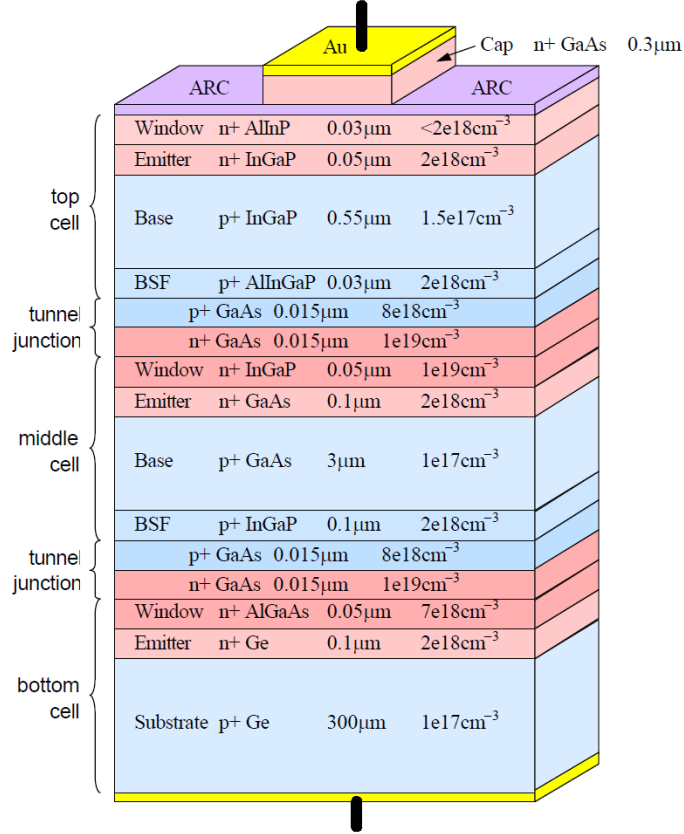


Figure 8. Example Triple Junction Solar Cell. Source: [1].

4. Current Multi-junction Cell Records

The current record holder for solar cell efficiency is held by the Fraunhofer ISE/Soitec concentrator-type photovoltaic multi-junction solar cell at 46% efficiency. The cell, independently verified by AIST in Japan, is a wafer-bonded GaInP/gallium arsenide (GaAs)/allium indium arsenide phosphide (GaInAsP)/GaInAs four-junction (4-J) cell under a 508-fold concentration of AM 1.5d spectrum sunlight with a fill factor of 85.1% and efficiency of 46% [17]. The concentrated nature of the system, utilizing mirrors that focus sunlight, allows for usage of higher intensities of the terrestrial spectrum, which increases cell efficiency higher than that normally possible. The cell was grown using lattice-matched epitaxial growth that allowed for low threading dislocation densities [17]. The IV characteristic curve for the 5.2 mm² designated cell area is shown in Figure 9,

while the EQE for each of the junctions is shown in Figure 10. The peak EQE for each junction is $> 90\%$ with an average current density $> 13 \text{ mA/cm}^2$ for each junction.

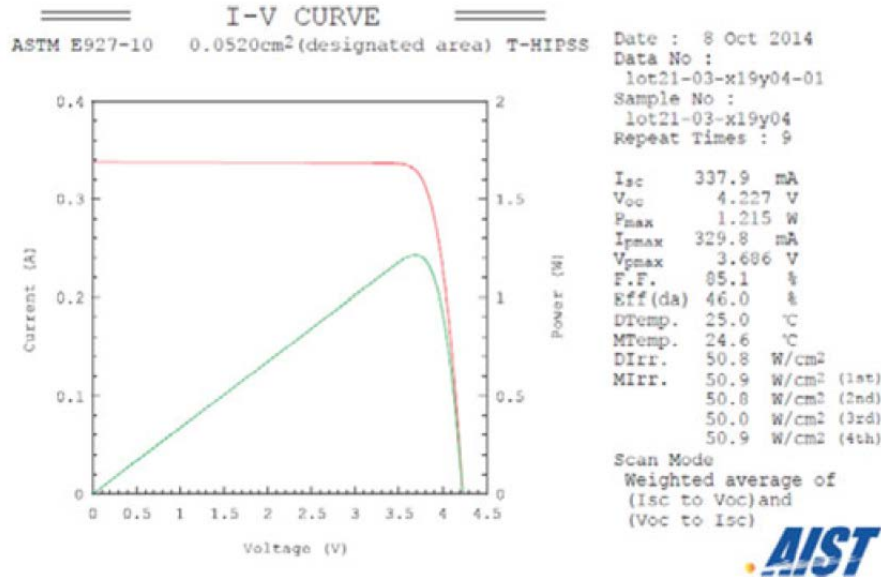


Figure 9. Fraunhofer ISE / Soitec Concentrator 4-J Solar Cell Record Holder IV Characteristic. Source: [17].

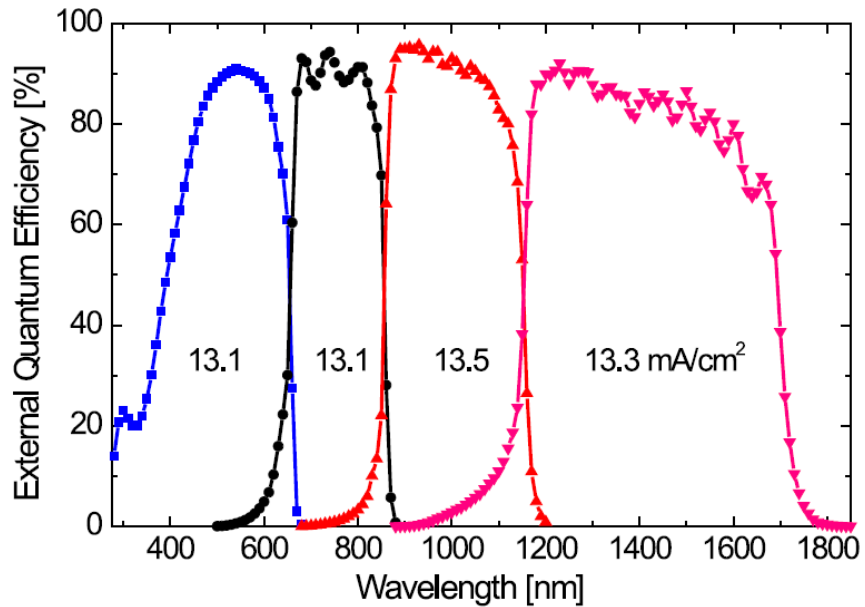


Figure 10. Fraunhofer ISE / Soitec Concentrator 4-J Solar Cell Record Holder EQE. Source: [17].

For non-concentrator photovoltaics, the current record is the Boeing-Spectrolab five-junction (5-J) direct bonded cell at 38.8% efficiency at one sun under the AM 1.5G spectrum at 25°C [18]. Using a Veeco K475 metalorganic vapor phase epitaxy (MOVPE) system, Boeing-Spectrolab grew the top three junctions lattice-matched to GaAs, while the bottom two junctions were grown upright on indium phosphide substrates [18]. These cells were then wafer bonded together to form the full five-junction cell. The NREL-measured IV characteristic curve for the 1 cm² designated cell area is shown in Figure 11, while the EQE (shown in blue) along with the internal quantum efficiency and reflectance for each of the junctions is shown in Figure 12. The peak EQE for each junction, with the exception of the second junction, is $\geq 90\%$ with an average current density $> 9.6 \text{ mA/cm}^2$ for each junction.

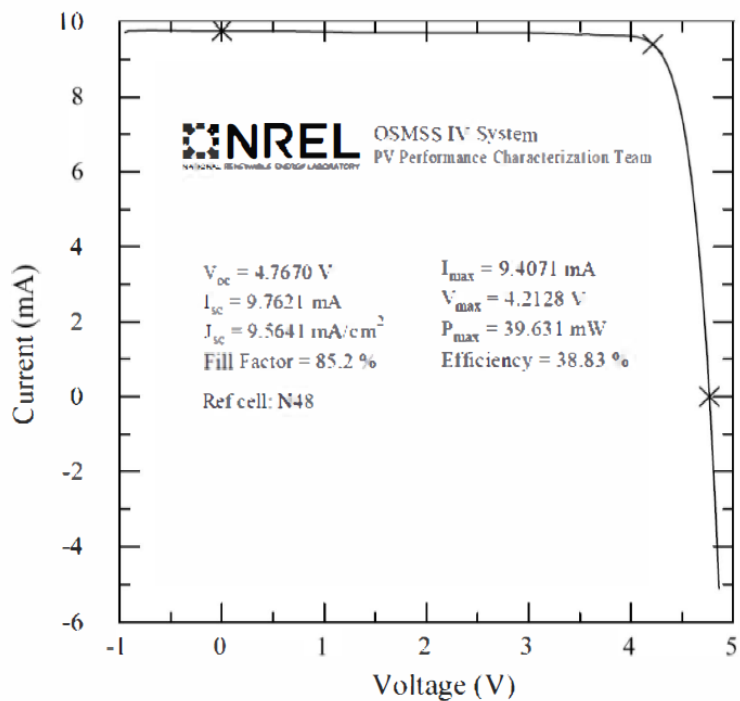


Figure 11. Boeing-Spectrolab 5-J Solar Cell Record Holder IV Characteristic.
Source: [18].

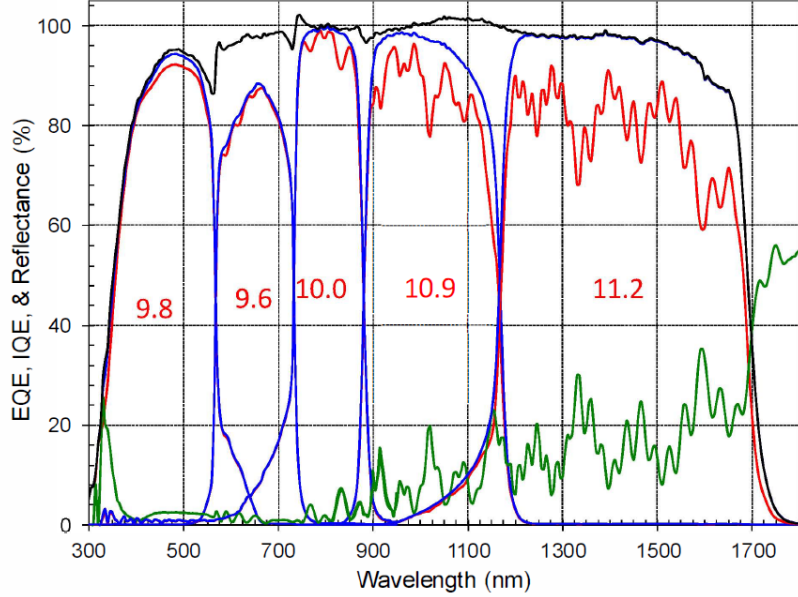


Figure 12. Boeing-Spectrolab 5-J Solar Cell Record Holder EQE. Source: [18].

C. SOLAR CELL DESIGN OPTIMIZATION

Numerous techniques are available to optimize solar cell designs to achieve maximum output power and efficiency. Tweaking parameters by hand through trial and error is one crude and inefficient method that requires the least knowledge of optimization techniques but can lead to the longest optimization timeline with questionable results. Genetic algorithm optimization was previously utilized at NPS by Bates, Tsutagawa, and Utsler with successful results [2], [4], [5]. Püschel recently demonstrated the effectiveness of nearly orthogonal Latin hypercube (NOLH) design-of-experiments optimization utilizing Tsutagawa's dual-junction cell [7]. Genetic algorithm optimization and NOLH are briefly discussed.

1. Genetic Algorithms

Genetic algorithms utilize a survival-of-the-fittest principle as a metaheuristic to optimize different solar cell parameters based on random generation of initial parameters. It is an iterative, stochastic nonlinear process that does not rely on strict mathematical formulation [19]. With regard to solar cells, parameters such as doping concentration and layer thickness are seen as genes in a “chromosome”. A fitness function is generated

following parent chromosome execution in the simulation environment that defines the inferior solutions and best solutions in the design. Values that are seen as providing the best output from prior generations are kept, while inferior values are left behind. Bates utilized four binary bits to describe each of the parameters, leading to 16 different values that each parameter could take [2]. An example chromosome utilized by Bates is shown in Figure 13.

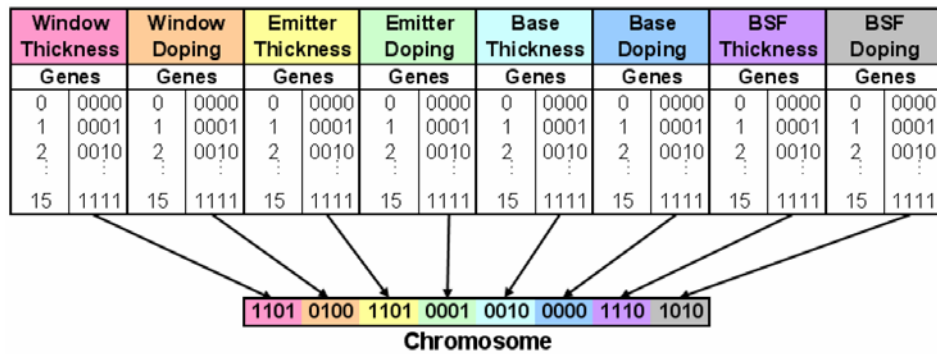


Figure 13. Example Chromosome Utilized by Bates. Source: [2].

For a cell layer with a window, emitter, base, and BSF and varying only thickness and doping concentration, 2^{32} , or 4,294,967,296, different combinations are possible. For the cell explored in this thesis, when not counting tunnel junctions, there are 23 different layers to be varied. Taking doping concentration and thickness for each layer (minus substrate thickness) as four bit values leads to 2^{180} different combinations. After a successful simulation iteration for the parents, crossover mixing of the parent chromosomes occurs to pass along successful genes along with bit-inverting mutations to add genetic variety [2]. Tsutagawa increased the size of the genes to seven bits to increase the design space available and adjusted mutation and crossover rates compared to Bates [4]. The designer specifies how many generations to proceed through before determining if an optimum has been reached.

Genetic algorithms as a method of optimization were not utilized in this thesis due to the size of the chromosomes required for implementation and the run time required to achieve an optimum result. Tsutagawa's genetic algorithm had runs from six to 102 hours

with solution spaces for single-junction solar cells of 1280 factorial and spaces for dual-junction cells of 2560 factorial [4]. Implementing such an algorithm for the baseline five-junction cell in this thesis would be overly complex and time-consuming due to the number of parameters involved.

2. NOLH/NOB Design of Experiments Optimization

Design-of-experiments (DoE) techniques seek to determine the optimum of a design space by taking a set of factors for a given system and describing the relationships between the factors via an appropriate sampling of the design space. Systematically finding the factors with the greatest effects on output parameters and the ways those factors' values correlate with other factors in the experiment allows for the determination of the optimum design point without an explicit requirement for iterative runs. Latin hypercubes are a method of populating the design space for DoE that seek to fill out the design space at more locations than just the center, faces, and corners by identifying unknown response surfaces with localized effects and complex interactions [20]. When no correlation exists between the input variables, the Latin hypercube is referred to as an orthogonal Latin hypercube, whereas a Latin hypercube with a maximum absolute pairwise correlation no greater than 0.05 between any two input variables is known as a NOLH [20]. Nearly orthogonal-balanced (NOB) DoE additionally allows for a mix of categorical and discrete input factors [21]. Utilizing NOLH/NOB designs prevent the designs from suffering detrimental multicollinearity effects. MacCalman's implementation of NOLH design allows for accounting for both first and second-order relations between input variables with minimal correlation [21]. The pre-generated values and second-order nature set the optimization method apart from traditional genetic algorithm optimization. Setting the design space in this fashion allows for finding the input factors that have the most influence on cell efficiency and how varying parameters affects other input factor contributions. For these reasons, NOLH/NOB DoE was selected as the method of optimization for this thesis research.

THIS PAGE INTENTIONALLY LEFT BLANK

III. EXPERIMENTAL DESIGN

A. MODEL BASELINE—FRAUNHOFER ISE 5-J CELL

The cell chosen as an initial baseline for the model designed in this research was developed by Fraunhofer ISE and first presented at the European Photovoltaic Solar Energy Conference in Munich in 2001 [8]. Key parameters that were focused upon for the Fraunhofer ISE cell design were lightweight materials for minimizing cell footprint on the satellites and radiation hardness to prevent device degradation from high-energy particle irradiation [9]. Dimroth et al. found that reducing the thickness of the base or emitter layers to less than the diffusion length after degradation lowered the degradation of the solar cell performance. The layout shown in Figure 14 was developed using MOVPE growth and process methodology on an AIX2600-G3 reactor and was an improvement from the iterations discussed in [8]. Through internal simulations using Fraunhofer's ETA-OPT software and by varying the bandgaps of the first and third cells, Dimroth et al. achieved a maximum efficiency of 43.5%. Due to the particular combination presenting insufficient crystal quality when lattice-matched to Ge, the group chose the more realistic material layout of Figure 14 with a simulated maximum efficiency of 40.8% using ETA-OPT [9].

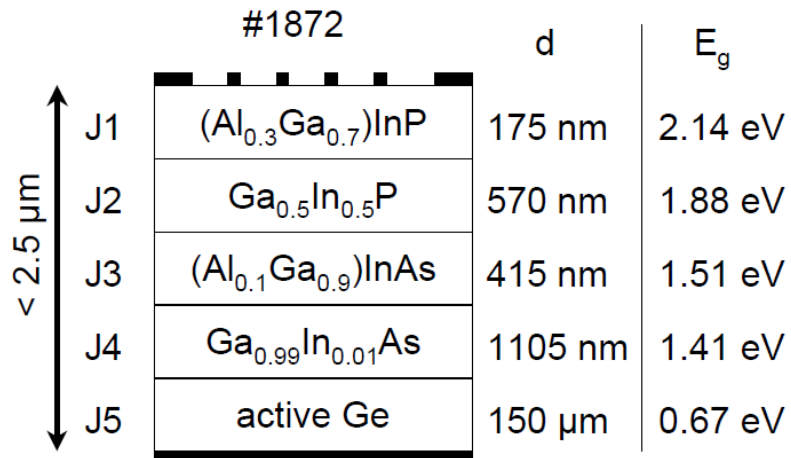


Figure 14. Fraunhofer ISE 5-J Solar Cell #1872 with Improved Radiation Hardness.
Source: [9].

The cells illustrated in Figure 14 are connected in series utilizing four separate tunnel junctions with highly-doped opposite polarity sides. In order to achieve peak tunneling current density, the tunnels between the first three cells have sides of p^+ aluminum gallium arsenide (p^+ -AlGaAs) and n^+ -GaInP, whereas the tunnel junction between J4 and J5 have sides of p^+ -AlGaAs and n^+ -GaInAs [9]. Although [9] mentions that the entire layout of the multi-junction cell is more than 30 layers, the specifics of each of the layers outside of majority-material makeup and thickness for each junction is not discussed in that work.

The measured EQE for the fabricated 5-J solar cell before and after irradiation (with the exception of the Ge layer only showing before irradiation) with 1.0-MeV electrons at 10^{15} cm^{-2} is shown in Figure 15. The first three junction layers have EQEs of $\leq 70\%$, while the final two junction layers have EQEs $\leq 90\%$.

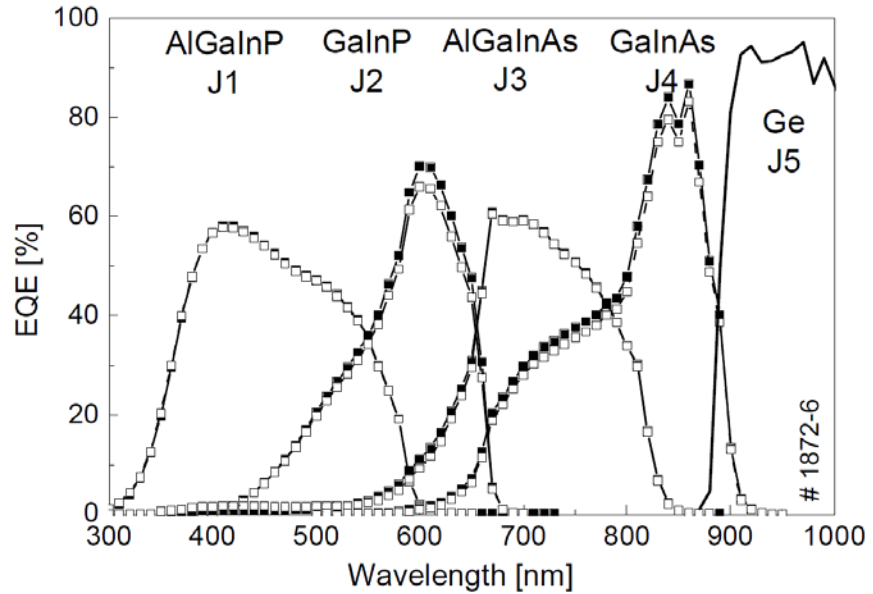


Figure 15. 5-J Cell EQE before and after 1 MeV Irradiation. Source: [6].

Dimroth et al. found the 5-J cell to maintain 93% of its initial efficiency, $\geq 94\%$ of J_{sc} , and $\geq 95\%$ of V_{oc} as compared to a similar 3-J cell maintaining 88% of its initial efficiency, $\geq 85\%$ of J_{sc} , and $\geq 95\%$ of V_{oc} after electron irradiation. It was concluded that

the 5-J structure performs similarly to a 3-J structure while outperforming the 3-J structure with regard to radiation resistance [9].

The absolute efficiency of the 5-J makeup was between 20% and 24% under the AM0 spectrum, while V_{oc} was around 5.2 V [9]. The IV characteristic for the 5-J cell is shown in Figure 16, with the GaInP current-limited curve representing the cell configuration. Dimroth et al. found the limitations in performance to be attributed to three things: losses due to reflection and absorption in the tunnel junctions, insufficient peak tunneling current densities in the high bandgap tunnel junctions, and low performance of the top AlGaInP top cell coupled with low shunt resistance. The low shunt resistance was attributed to insufficient purity of precursors used for growth or moisture or oxygen from gaseous or metalorganic sources degrading the MOVPE-grown layers [9].

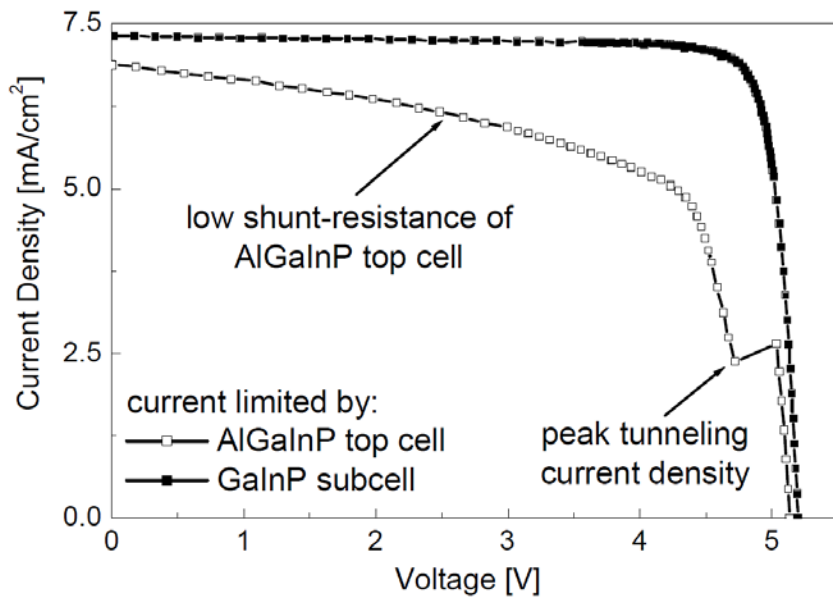


Figure 16. IV Characteristic of Fraunhofer ISE 5-J Solar Cell Used for Modeling.
Source: [9].

The 5-J solar cell discussed above was chosen as a baseline for this work for a variety of reasons. First, the majority-makeup of each of the layers is readily available. Each quaternary alloy included has the mole fractions given along with the reason for why the material was chosen. Additionally, the specific thicknesses the developers used

along with the material bandgaps are readily available in the published papers. For a large portion of solar cells available today, specific information is withheld for proprietary reasons so that the specifics cannot be repeated for commercial gain.

Another consideration leading to the selection were the materials themselves. The optical parameters consisting of refractive index and extinction coefficient values are not readily compiled for every material currently being utilized in solar cells. Although such optical parameters are readily available for unary materials such as Ge or binary materials such as GaAs, the more complex ternary and quaternary semiconductors need to be compiled on a case-by-case basis through complex interpolation methods. The materials utilized in the Fraunhofer ISE multi-junction cell have refractive index files that are either readily available in Silvaco's SOPRA index or can be compiled via data readily available online. When exact matches for the material refractive index files are not available for the structure, close substitutes that differ by a small mole fraction are available.

B. MODEL DEVELOPMENT AND BASELINE

1. Model Development Procedure

Silvaco's ATLAS suite allows users to model via two-dimensional and three-dimensional simulation the behavior of semiconductor devices such as IGBTs, power diodes, and solar cells [22]. The user defines an “input deck” that is interfaced by Silvaco Atlas with different libraries and databases to model the particular semiconductive device. This is performed by discretizing the semiconductor transport equations over a defined mesh on top of a device design, allowing the semiconductor transport equations to be solved under varying bias conditions.

a. Mesh Generation

The input deck is first established by specifying a two-dimensional mesh for the structure with each of the layers and tunnels specified. The flexibility in the meshing definition allows either the explicit dictation of the positioning of each layer micron by micron or automeshing according to what regions are defined. Specifying the spacing

between the different layers (essentially defining how coarse or fine the mesh is) directly correlates to the accuracy and simulation time of the deck dependent on the specified models (Gummel, Newton, etc.).

The mesh specified for the solar cell simulations in this thesis research was dynamically generated initially. The spacing was modeled as a percentage of the layer thickness. Proceeding in this manner ensured that the spacing would not be too little or too much as the optimization varies the layer thicknesses. When convergence issues presented themselves in a large portion of the simulation runs, the spacing was reduced to below the lower bounds of the layer thickness specified in the NOB spreadsheet for the particular input factor, ensuring that adequate spacing was guaranteed across the structure but increasing simulation computation time.

b. Region Definitions and Doping

The next step was to define the material regions that correspond with the defined meshing for each layer. Each region is bound with precise location points defining a top position where the region starts and a lower position where the region ends. Alternatively, when automeshing the input deck, implicit positioning can also be utilized where one region can be defined as existing beneath another without defining specific starting and ending locations. Having the region definitions not coincide with the meshing leads to inaccurate and erratic behavior and can lead to the simulation outright failing. For this thesis research, explicit definition of the meshing and material regions was utilized due to the automeshing defining too fine an area when such accuracy was not needed, leading to large simulation times. Along with the position of each region, the material makeup was defined (AlInP, GaInP, etc.). Regions defined with a given material behave according to the material parameters defined later in the input deck. The doping was also defined for each material region. Uniform doping was prescribed along with the doping type (n or p) and the specific concentration.

c. Electrodes/Contacts

After defining the material regions, electrodes were established across the cell with positions corresponding to the mesh and region statements defined earlier in the

input deck. The cathode was attached to the top of the first cell's first n-type layer, and the anode was attached to the bottom of the last cell's bottom p-type layer. Additional electrodes were defined for each side of each tunnel junction as discussed in [3] due to QTREGION statements not being utilized. Each side of the tunnel was given a high resistance value (10^{14} - 10^{17} Ω) to allow current flow with low loss through the region and to isolate the electrode specified from ground. The materials specified in the tunnel regions maintain the optical properties specified in the material statements, allowing light to travel through the regions uninhibited. Having resistance be too small reduces the current density via the parasitic path to ground presented by the resistor. For the input deck utilized in this thesis research, the cumulative resistance in series across all of the tunnel junctions is 10^{17} Ω , leading to 0.125×10^{17} Ω for each side of each tunnel.

d. Tunnel Junctions

Tunnel junctions can be defined a number of ways. One method is to define a rectangular mesh for the quantum tunneling current to be calculated across the tunnel using QTREGION, QTX.MESH, and QTY.MESH statements [22]. When trying to utilize this method, one must enable non-local band-to-band tunneling in the modeling section. Enabling the model gives a more accurate simulation by modelling the forward and reverse tunneling currents of degenerately doped p-n junctions vice calculating recombination-generation based on field values local to a given point [22]. This method of tunnel modelling worked well for dual-junction solar cells when building up to the five-junction simulation; however, adding more than one QTREGION when adding an additional tunnel led to erratic and unexpected behavior that could not be rectified. A workaround first utilized by Tsutagawa after discussion with Silvaco was employed that makes the tunnel a perfect conductor vice modelling accurate tunnel junctions [3]. This allowed simulation of the multi-junction cell to a fairly accurate degree compared to the experimental results achieved by Fraunhofer ISE.

e. Material Definition

Each of the different materials used in the simulation and their individual properties are defined via the material statements. Specific values utilized in the input deck are given in Tables 1 and 2. Each of the individual parameters is discussed.

Table 1. Material Parameters Used in Input Deck

Material	Bandgap @ 300 K (eV)	Permittivity (F/cm)	Affinity (eV)	MUN (cm ² /V·s)	MUP (cm ² /V·s)	Refractive index file with n and k values over given λ
AlInP	2.4	11.7	4.2	2291	142	Againp10.nk
(Al _{0.3} Ga _{0.7})InP	2.1744	12.16	4.26	1000	500	Againp3_test_271.nk
GaInP	1.9	11.8	4.09	1945	141	solarex03.nk
(Al _{0.1} Ga _{0.9})InAs	1.51	12.8	3.96	3000	150	algaas_mod.nk
Ga _{0.99} In _{0.01} As	1.41	13.12	4.08	3000	150	Ringas.all
GaAs	1.424	12.9	4.07	8500	400	Gaas.nk
Ge	0.66	16.2	4	3900	1800	Ge.nk

Adapted from [1], [6], [12], [22], [23], [24], [25], [26], [27].

Table 2. Material Parameters Used in Input Deck Continued

Material	NC @ 300 K (cm ⁻³)	NV @ 300 K (cm ⁻³)	AUGN	AUGP	COPT	TAUN	TAUP
AlInP	1.08×10 ²⁰	1.28×10 ¹⁹	5.447×10 ⁻³⁰	2.957×10 ⁻²⁹	1.0×10 ⁻¹⁰	1.0×10 ⁻⁶	1.0×10 ⁻⁶
(Al _{0.3} Ga _{0.7})InP	9.13×10 ¹⁷	7.81×10 ¹⁸	-	-	1.5×10 ⁻¹⁰	1.0×10 ⁻⁹	2.0×10 ⁻⁸
GaInP	6.55×10 ¹⁷	1.5×10 ¹⁹	3.0×10 ⁻³⁰	3.0×10 ⁻³⁰	1.0×10 ⁻¹⁰	4.0×10 ⁻⁹	4.0×10 ⁻⁹
(Al _{0.1} Ga _{0.9})InAs	6.54×10 ¹⁷	1.12×10 ¹⁹	3.0×10 ⁻³⁰	3.0×10 ⁻³⁰	1.0×10 ⁻¹⁰	1.0×10 ⁻⁶	1.0×10 ⁻⁶
Ga _{0.99} In _{0.01} As	3.93×10 ¹⁷	9.1137×10 ¹⁸	3.0×10 ⁻³⁰	3.0×10 ⁻³⁰	1.0×10 ⁻¹⁰	1.0×10 ⁻⁹	1.0×10 ⁻⁹
GaAs	4.7×10 ¹⁷	9.0×10 ¹⁸	1.0×10 ⁻³⁰	1.0×10 ⁻³⁰	1.0×10 ⁻¹¹	5.1×10 ⁻⁷	5.1×10 ⁻⁷
Ge	1.04×10 ¹⁹	6.0×10 ¹⁸	1.0×10 ⁻³⁰	1.0×10 ⁻³⁰	6.41×10 ⁻¹⁴	3.8×10 ⁻³	3.8×10 ⁻³

Adapted from [1], [6], [12], [22], [23], [24], [25], [26], [27].

(1) Bandgap

The bandgap of the material is dependent on the bandgaps of the individual elements making up the material, their mole fractions, and their bowing parameters. Obtaining correct bandgaps for each of the materials proved to be a more complex task than simply searching in one database. For this thesis research, the bandgaps used for AlInP, GaInP, GaAs, and Ge, respectively, were 2.4 eV, 1.9 eV, 1.424 eV, and 0.66 eV [1], [6]. The bandgap of $(Al_{0.3}Ga_{0.7})InP$ (2.1744 eV) was calculated by [23]

$$E_g^{Al_zGa_{(1-z)}InP} = [2.007(1-z) + 2.691z - 0.18z(1-z)] \quad (12)$$

where z corresponds to the mole fraction of Al (0.3). The bandgap of $(Al_{0.1}Ga_{0.9})InAs$ (1.51 eV) was calculated according to [23]

$$\begin{aligned} E_g^{(Al_xGa_y)In_{(1-x-y)}As} = & x(E_g^{AlAs}) + y(E_g^{GaAs}) + (1-x-y)E_g^{InAs} - xy(K^{AlGaAs}) \\ & - y(1-x-y)K^{GaInAs} - x(1-x-y)K^{AlInAs} \end{aligned} \quad (13)$$

where $x=0.1$, $y=0.9$, and K corresponds to the compound's bowing parameter for the Γ -valley [23], [24]. The bandgap of $Ga_{0.99}In_{0.01}As$ (1.41 eV) was calculated according to [6], [23], [24]

$$E_g^{Ga_xIn_{(1-x)}As} = x(E_g^{GaAs}) + (1-x)E_g^{InAs} - x(1-x)K^{GaInAs} \quad (14)$$

where $x = 0.99$.

(2) Permittivity and Affinity

A material's relative permittivity describes the factor by which the electric field between two charged particles decreases relative to the permittivity of vacuum. The electron affinity is defined as the energy required for an electron to be taken from the bottom of the conduction and moved to a position just outside of the material [12]. Values for each compound's permittivity and affinity were gathered from various sources or calculated using approximations relative to the constituent compounds' mole fractions and permittivity/affinity values [1], [6], [23].

(3) Electron and Hole Mobility

As the doping concentration of a material is modified, the electron and hole mobilities of a material change accordingly. The ease of flow and its change with the parameters vary according to the material chosen. Mobility selection for each material follows the method used by Michalopoulos [1]. The mobilities for GaAs were specified by power law temperature dependence and obtained by interpolation, with the interpolated values being used for each material's mobilities [1], [22]. Due to the CONMOB model in Silvaco Atlas only specifying mobilities specifically for materials called out as Si and GaAs, the mobilities must be manually entered into each material's parameters as they do not make use of the CONMOB directly. The default values for electron and hole mobilities when CONMOB or manual mobility declaration are not used are $1000 \text{ cm}^2/\text{V}\cdot\text{s}$ and $500 \text{ cm}^2/\text{V}\cdot\text{s}$, respectively.

(4) Refractive Index

The refractive index file describes the refractive index and extinction coefficient for a given material over a range of wavelengths. Silvaco provides a database of refractive index data from SOPRA, a thin film meteorology company that compiled the numerous material optical parameter values. Although many of the materials' refractive index files used in the input deck can be readily accessed via the SOPRA database in Silvaco ATLAS or Silvaco ATLAS example files (AlInP, GaInP, $\text{Ga}_{0.99}\text{In}_{0.01}\text{As}$, GaAs, Ge), other materials had issues with extinction coefficient existing past the bandgap energy $[(\text{Al}_{0.3}\text{Ga}_{0.7})\text{InP}]$ or questionable values $[(\text{Al}_{0.1}\text{Ga}_{0.9})\text{InAs}]$. In the case of $(\text{Al}_{0.3}\text{Ga}_{0.7})\text{InP}$, the refractive index file was modified by taking the value of the extinction coefficient at the bandgap and subtracting that value from the rest of the values of the extinction coefficient so that the value would be zero at the bandgap and beyond. The values for $(\text{Al}_{0.1}\text{Ga}_{0.9})\text{InAs}$ were provided by Aspnes for AlGaAs between $0.2066 \mu\text{m}$ and $0.8266 \mu\text{m}$ [25]. In order to match the bandgap derived by Dimroth et al. for the material, the percentage of indium in $(\text{Al}_{0.1}\text{Ga}_{0.9})\text{InAs}$ was reduced to zero, essentially leaving the material as AlGaAs.

(5) Effective Density of States

The effective density of states for holes (NC) and electrons (NV) refer to the integrated concentration of available states in the conduction and valence bands that can be occupied at a given temperature T . $NC300$ and $NV300$ describe the density of states at 300 K. Using the effective masses for electrons (m_e^*) and holes (m_h^*), the effective density of states at $T=300$ K are given by [12]

$$NC = 2 \left(\frac{2\pi m_e^* k T}{h^2} \right)^{3/2} \quad (15)$$

and

$$NV = 2 \left(\frac{2\pi m_h^* k T}{h^2} \right)^{3/2} \quad (16)$$

with h being Planck's constant in joule-seconds and k being the Boltzmann constant in joules per Kelvin. The values for $(Al_{0.1}Ga_{0.9})InAs$ and $Ga_{0.99}In_{0.01}As$ were calculated in this manner using particle parameters from Levinstejn [26]. Values that could not be easily calculated due to not having accurate effective particle masses on hand were obtained from various sources [1], [6], [27].

(6) Models and Associated Parameters

Numerous models of secondary physical effects are important when simulating solar cell operation to increase the accuracy and validity of the Silvaco ATLAS simulation.

The SRH recombination model concerns trap-assisted recombination. Impurities in the lattice of a semiconductor create energy states in the bandgap that trap electrons and holes that can then recombine with the opposite carrier. The recombination process is described by [22]

$$R_{SRH} = \frac{pn - n_{ie}^2}{\tau_p \left(n + n_{ie} e^{\frac{E_F - E_T}{kT_L}} \right) + \tau_n \left(p + n_{ie} e^{\frac{-(E_F - E_T)}{kT_L}} \right)} \quad (17)$$

where τ_n and τ_p are electron and hole lifetime parameters (TAUN and TAUP in Silvaco Atlas), n_{ie} is a spatially varying intrinsic concentration level, E_i is the intrinsic Fermi energy level, E_T is the trap energy level, and T_L is the lattice temperature in Kelvin.

The Auger recombination model qualitatively describes when an electron gains energy from the recombination of a hole and electron rather than the energy simply being given up as a photon. The excited electron collides within the lattice, giving up its energy to other electrons and holes before ending up back in the conduction band. The Auger recombination process is described by [22]

$$R_{Auger} = \Gamma_n (pn^2 - nn_i^2) + \Gamma_p (np^2 - pn_i^2) \quad (18)$$

where Γ_n and Γ_p are Auger parameters (AUGN and AUGP in Silvaco ATLAS). The recombination is highly dependent on the carrier concentration within the material.

The OPTR model simulates band-to-band radiative recombination that takes place in the drift-diffusion part of the simulation of a semiconductor [18]. No radiative effects concerning photon generation are included in this model, so band-to-band recombination does not affect photon transport through the device. The recombination is given by [22]

$$r = R_r (np - n_i^2) \quad (19)$$

where R_r is the radiative recombination rate (COPT in Silvaco Atlas).

Specifying Fermi in the models statement ensures that Fermi-Dirac statistics are used. These statistics describe how an electron behaves in a semiconductor lattice when in thermal equilibrium. Usage of the Fermi-Dirac statistics “account for reduced carrier concentrations in heavily-doped emitter layers... adjacent to Ohmic contacts” [6].

The bandgap narrowing model *bgn* accounts for the bandgap narrowing that occurs in highly-doped materials ($>10^{18} \text{ cm}^{-3}$). Bandgap narrowing takes place due to the effects of heavy doping upon the electronic structure of a semiconductor. The effect of narrowing is to modulate the intrinsic carrier concentration according to [22]

$$n_{ie}^2 = n_i^2 e^{\frac{\Delta E_g}{kT}} \quad (20)$$

where T is the temperature and n_i is the intrinsic level.

Values for AUGN, AUGP, COPT, TAUN, and TAUP were derived from various experimental sources [1], [4], [6].

f. Numerical Method

The method selected for solving the non-linear equations that make up the simulation can be user specified with the method call. For this thesis research, Newton's method was utilized. The method iteratively solves a linearized version of the non-linear semiconductor transport characteristic equations [22]. As long as the initial guess is close to the final solution, the problem should converge relatively quickly [22]. Newton's method is the default method selected for solving the drift-diffusion problems in the software.

g. Beam Statement

The beam statement selects the specified light spectrum of the source to which the multi-junction solar cell is exposed. It specifies the position the light beam originates, the starting and ending optical wavelengths for the beam, the number of points to use between the starting and ending wavelengths, and the light spectrum being used (AM0 for space, AM1.5 for terrestrial, etc.). Multiple beam statements can be made in order to analyze the EQE data for each cell junction. Example Silvaco ATLAS code for determining EQE for a given cell is shown in Appendix A.

h. Parameter Extraction

After the light beam is declared, the initial solution for potential and carrier concentrations with no beam shining is calculated. The beam of light is then introduced into the simulation gradually in order to aid with problem convergence. If the problem cannot converge after ten attempts at 40 iterations each, Silvaco ATLAS moves on to the next statement. After the beam problem has been solved, the IV characteristic curve can be derived by sweeping from zero volts to whatever voltage the user specifies to end.

Extract statements can be utilized to determine parameters of interest for the cell function. For this thesis research, J_{sc} , V_{oc} , P_{max} , fill factor, and efficiency are extracted along with the general IV characteristic curve.

The EQE extraction is performed using the method described by Thériault [28]. Biasing beams corresponding to just below the bandgaps of the cells not having their EQE examined are shined on the multi-junction solar cell in order to excite the layers. Another beam is then swept over a given wavelength spectrum that covers the band gaps of the individual layers. The values of the biasing beam currents are then subtracted from the swept beam's current to isolate the cell part in which we are interested. This is performed a number of times corresponding to the number of cells from which EQE must be extracted. Sample code for gathering EQE from the first cell is shown in Appendix A. Due to difficulties in isolating EQE for Cells 3 and 4 separately, the EQE data for those two cells is gathered together. The deck was required to be run on a Linux machine in order to utilize 128-bit precision when attempting beam convergence via Newton's method. The 128-bit precision for Silvaco ATLAS is not available on Windows platforms.

2. Baseline Cell

For the baseline cell modeling the Dimroth et al. five-junction solar cell, the configuration shown in Figure 17 was used. As the specifics for layer composition (windows, buffers, etc.) were not publically available, assumptions were made to aid in optimization while best representing the designed cell. Doping concentrations and thicknesses were chosen to match (within reason) the current density and open circuit voltage achieved by Dimroth et al. [9]. The different parts (window, emitter, base, BSF, and buffer) and initial doping concentrations were first modeled after Michalopoulos and then adjusted to ensure a sufficient J_{sc} and V_{oc} were obtained [1]. Materials with affinities and bandgaps similar to the majority makeup were selected. Additionally, it was necessary to restrict the mole fraction of alloys used to ensure that experimental parameters and refractive index values were available. The overall thickness for the baseline multi-junction cell, excluding the active Ge substrate at the bottom, was 2.525

μm, similar to the thickness of the cell fabricated by Dimroth et al. The baseline cell contains 31 layers, matching the “more than 30 layers” from the Dimroth et al. design [9].

Legend

AllnP
AlGaInP
AlGaInAs
GalnP
GaAs
InGaAs
Ge

Cathode

Window	n+	0.01 μm	2E18 cm ⁻³
Emitter	n+	0.02 μm	2E18 cm ⁻³
Base	p+	0.125 μm	1.5E17 cm ⁻³
BSF	p+	0.01 μm	2E18 cm ⁻³
Buffer	p+	0.01 μm	1E18 cm ⁻³
Emitter	p+	0.015 μm	8E18 cm ⁻³
Base	n+	0.015 μm	1E19 cm ⁻³
Window	n+	0.01 μm	2E18 cm ⁻³
Emitter	n+	0.07 μm	2E18 cm ⁻³
Base	p+	0.5 μm	1.5E17 cm ⁻³
BSF	p+	0.01 μm	2E18 cm ⁻³
Buffer	p+	0.1 μm	1E17 cm ⁻³
Emitter	p+	0.015 μm	8E18 cm ⁻³
Base	n+	0.015 μm	1E19 cm ⁻³
Window	n+	0.03 μm	2E18 cm ⁻³
Emitter	n+	0.03 μm	2E18 cm ⁻³
Base	p+	0.275 μm	1.5E17 cm ⁻³
BSF	p+	0.03 μm	2E18 cm ⁻³
Buffer	p+	0.03 μm	1E18 cm ⁻³
Emitter	p+	0.015 μm	8E18 cm ⁻³
Base	n+	0.015 μm	1E19 cm ⁻³
Window	n+	0.03 μm	2E18 cm ⁻³
Emitter	n+	0.05 μm	2E18 cm ⁻³
Base	p+	0.965 μm	1.5E17 cm ⁻³
BSF	p+	0.03 μm	2E18 cm ⁻³
Buffer	p+	0.03 μm	2E18 cm ⁻³
Emitter	p+	0.015 μm	8E18 cm ⁻³
Base	n+	0.015 μm	1E19 cm ⁻³
Window	n+	0.03 μm	2E18 cm ⁻³
Emitter	n+	0.01 μm	2E18 cm ⁻³
Substrate	p+	149.96 μm	1.5E17 cm ⁻³
Anode			

Tunnel 1

Tunnel 2

Tunnel 3

Tunnel 4

Cell 1

Cell 2

Cell 3

Cell 4

Cell 5

Figure 17. Baseline Multi-junction Solar Cell Configuration.
Adapted from [1], [9].

C. INPUT FACTOR SELECTION AND OPTIMIZATION USING NOB DOE

The NOLH/NOB design selected for filling the design space was developed by Vieira in Excel [29]. The spreadsheet is an NOB implementation that was used for this thesis research following the NOLH implementation spreadsheet utilized by Püschel, which only allowed for 29 input factors. A snippet of the spreadsheet used is shown in Figure 18. Low and high end bounds are set by the user along with the precision required. Once the factors are specified along with the bounds, 512 different run simulations were generated in order to populate the requested design space. To make the design space denser, the user has the ability to rotate and stack the input variables. Rotating involves taking the variables and bounds in one column and copying them one column over. This generates a different data set in the new column as different algorithms are applied to generate the data. Upon rotation completion, the new 512 runs are stacked onto the simulation execution queue, allowing a denser view of the specified input factor bounds. Rotating and stacking can be done as much as required or as time constraints allow.

lo	0.01	10	0.02
hi	0.09	1000	2
decimals	3	3	3
discrete levs			
factor name	topwinthick	topwindopco	topemthick
	0.016	943.816	0.357
	0.049	366.477	1.682
	0.039	874.07	0.101
	0.046	42.935	1.911
	0.074	984.501	0.365
	0.09	306.419	1.81
	0.081	443.973	0.283
	0.048	963.19	0.59
	0.02	232.798	1.833
	0.045	223.112	1.915

Figure 18. Spreadsheet Snippet from Vieira's NOB DoE Implementation.
Source: [28].

For factor selection, layer thickness and doping concentrations were varied for every active layer in each cell. Thickness values in the table correspond to micrometer values, and the doping concentrations are multiples of 10^{16} cm^{-3} . For example, a value of one in the doping concentration section equates to $1.0 \times 10^{16} \text{ cm}^{-3}$, and 351 equates to $3.51 \times 10^{18} \text{ cm}^{-3}$. The tunnel junction doping concentrations and thicknesses were held constant. Trying to find parameter correlations in the tunnel junctions leads to incorrect input factor relationships in the statistical model generated after the runs. The fifth cell substrate thickness was also not varied and was made sufficiently thick to best simulate real world solar cells with thick bottom substrates. The number of simulation runs (or design points) to populate the design space was chosen to be 1024 to ensure the total simulation runtime took around 24 hours or less on the simulation computer while still gathering enough data to construct a statistical model. Each 1024-count simulation run set is referred to as an iteration.

Once the 1024 simulation run values for the iteration were generated by the Excel spreadsheet, the values were copied into a comma-separated value (CSV) file. This CSV file was read by a Python preprocessing script, presented in Appendix B, in order to generate the 1024 Silvaco ATLAS input decks. Values in the Python script must be modified if more or less simulation runs than 1024 are required or if line spacing in the baseline input file (dimroth.in for this thesis research) is changed. The Python run script in Appendix B then called ATLAS from the kernel repeatedly to run the 1024 input decks in order and generate Data (DAT) files with output power information. Once the 1024 simulation runs were complete, a Python postprocessing script was executed to attach the output power from each simulation to its corresponding run, creating a new CSV file.

Once the CSV file with the output powers for the iteration was created, the data were fed into the JMP statistical software suite. From here, the distribution for the target parameter extracted from the simulation runs, the peak output power P_{max} , was viewed to determine the number of successful runs and see how the data was spread. A stepwise linear regression model was then applied with the input factors fit to linear and polynomial models and the role variable being the Sim Result. A higher number of successful simulation runs where the data converges tends to lead to better models and,

thus, the discovery of the most important input factors for the simulation. Once the model was built and run, a profiler was executed that allowed the designer to predict based on the statistical model what values of the cell parameters produced the optimal output power in the ATLAS model of the cell.

THIS PAGE INTENTIONALLY LEFT BLANK

IV. EXPERIMENTAL RESULTS

A. BASELINE RESULTS

The derived IV characteristic curve and power versus voltage for the simulated solar cell are shown in Figures 19 and 20, respectively. The derived values for the parameters of interest are shown in Table 3. A low fill factor of 69.3852% is indicated by the depressed maximum power point of the IV characteristic curve. The open circuit voltage of 5.26026 V compares favorably to the 5.2-V range seen in the Dimroth et al. multi-junction cell [9]. The efficiency 26.2166% is roughly 2% more than the Dimroth et al. cell due to the higher current displayed in the IV characteristic curve seen in Figure 19. The larger short circuit current compared to Dimroth et al. (9.80609 mA versus approximately 7.5 mA) is attributed to the use of ideal electrodes for the tunnel junctions, different materials used for the windows and buffers compared to the majority material for the cell, and refractive index and extinction coefficient values utilized for the simulation.

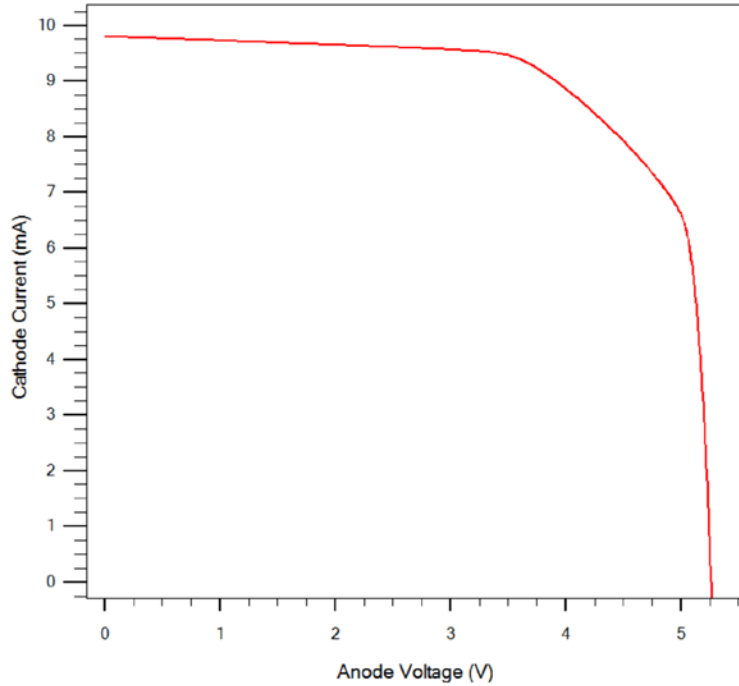


Figure 19. Baseline Cell IV Characteristic

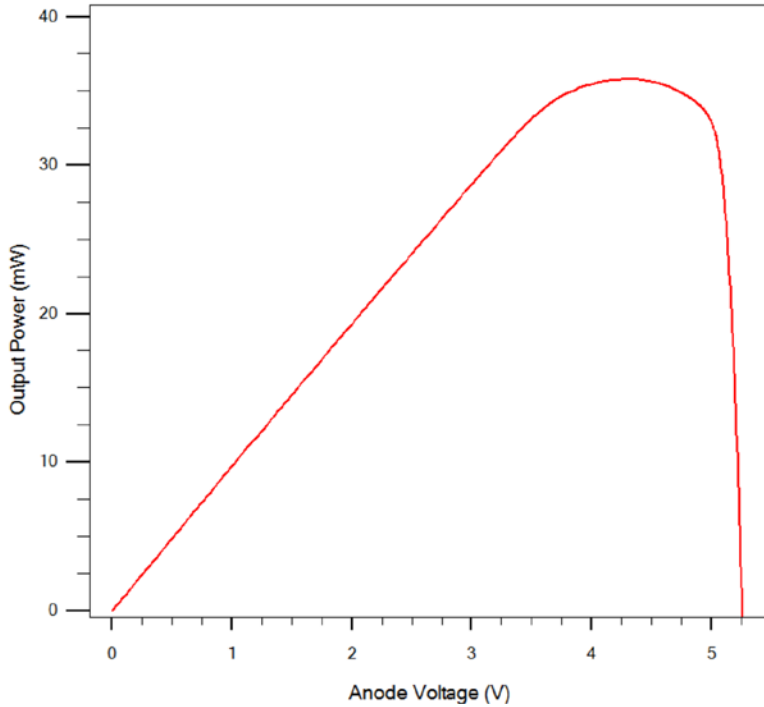


Figure 20. Baseline Cell Power versus Voltage

Table 3. Silvaco ATLAS Baseline Results

Parameter	Value
J_{sc}	9.80609 mA/cm ²
V_{oc}	5.26026 V
P_{max}	35.7907 mW/cm ²
FF	69.3852%
Efficiency	26.2166%

The EQE for the baseline cell can be found in Figure 21. The first two cell EQEs cap at approximately 62%. The EQE for the first cell is very close to the EQE of Dimroth's first cell, while the EQE for the second cell is approximately 8-10% less. Cells 3 and 4 have very small EQE with a maximum utilization of approximately 15%. This is largely due to the large tails for both cells 1 and 2, as shown in Figure 21. Photons are being absorbed in the higher layers prior to the photons reaching the lower layers, leading to the smaller EQE percentage. With regard to the Silvaco inputs, what this corresponds to is extinction coefficients existing in the refractive index files at wavelengths past the

bandgap of the materials. Although the files were modified where possible to minimize this, the effects are still present. The large tails also affect the EQE for cell 5, which maximizes its utilization at approximately 40%.

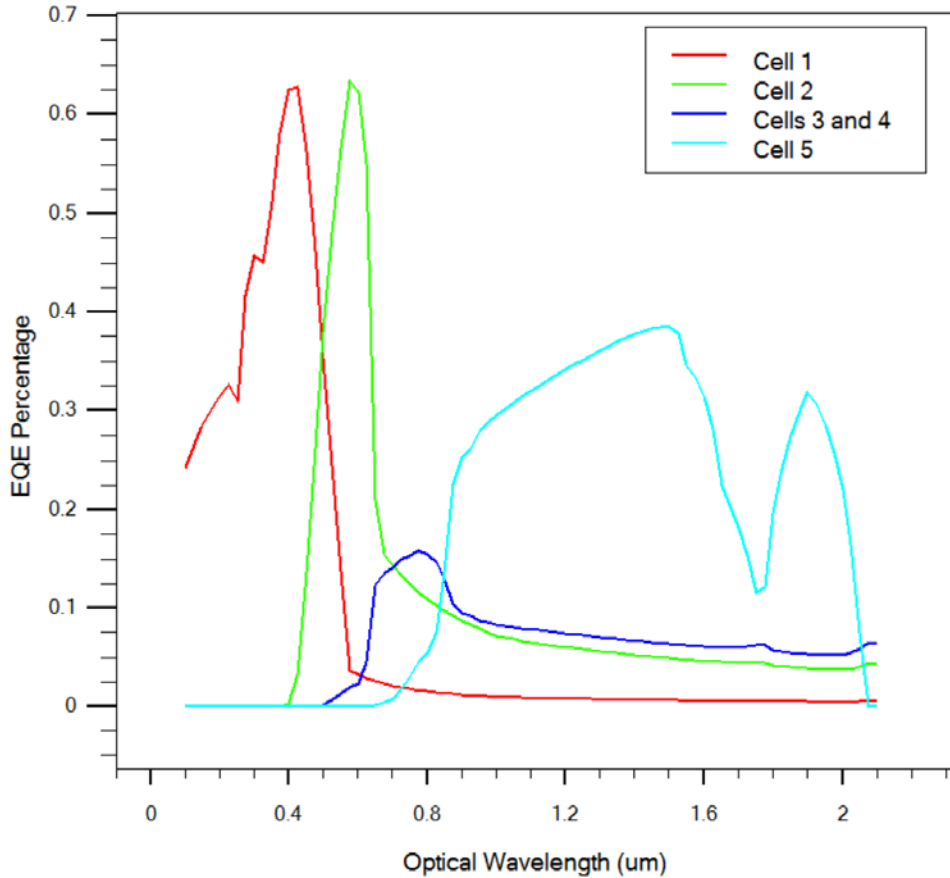


Figure 21. Baseline Cell EQE

A snapshot of the top three microns of the multi-junction cell and the electric fields generated on a logarithmic scale are shown in Figure 22. The tunnel regions are located at approximately 0.15 μm , 0.85 μm , 1.38 μm , and 2.48 μm in Figure 22. The majority of the fields are centered at the p-n junctions and near the buffer interface with the tunnels with little to no fields in the middle of the base regions. The material makeup is also shown in Figure 22 for reference.

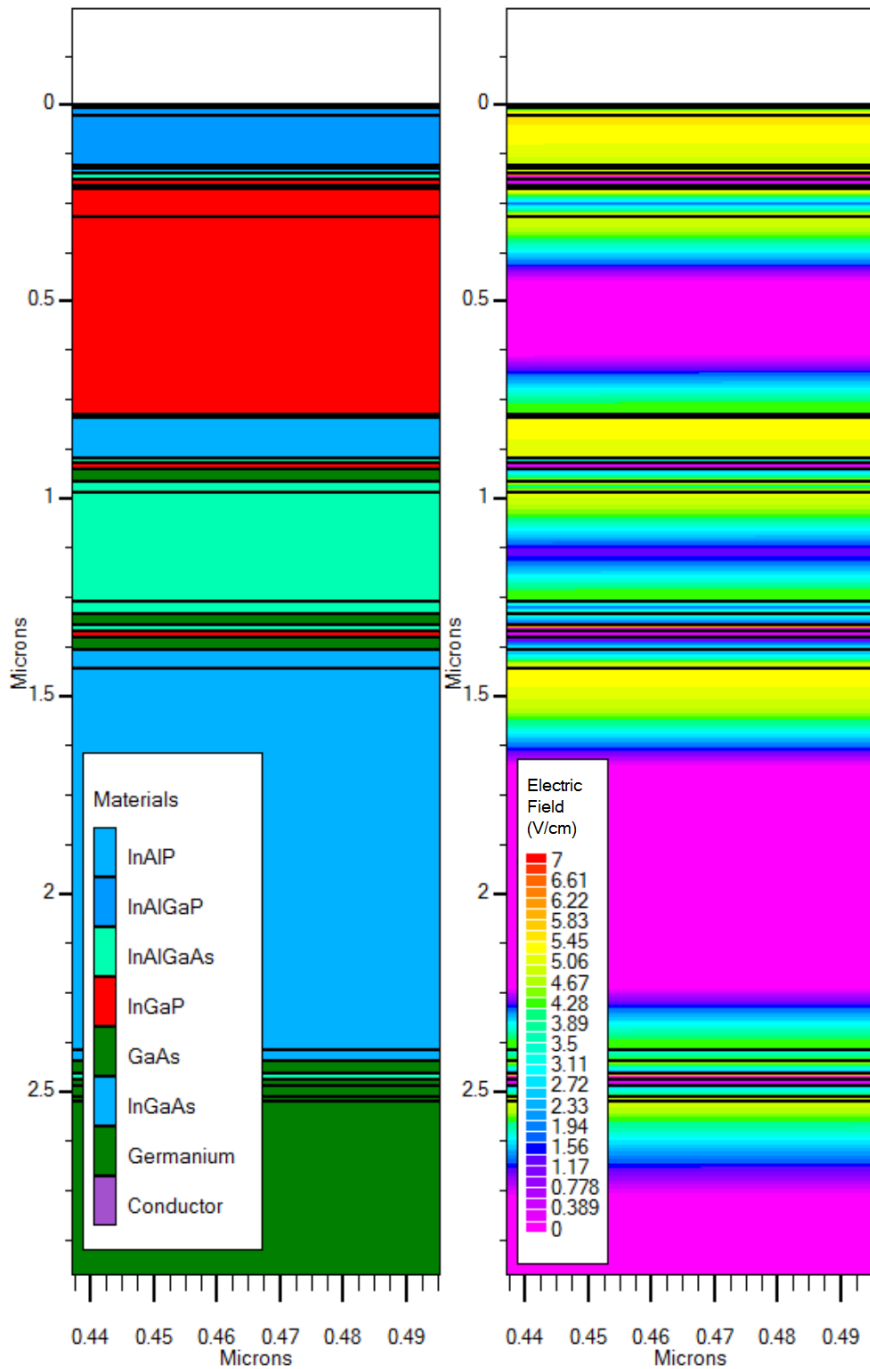


Figure 22. Electric Fields in Baseline Cell

The area of the multi-junction cell with the largest recombination rate is shown in Figure 23. Recombination rate is shown on a logarithmic scale with the second cell base exhibiting the largest rate near its p-n junction.

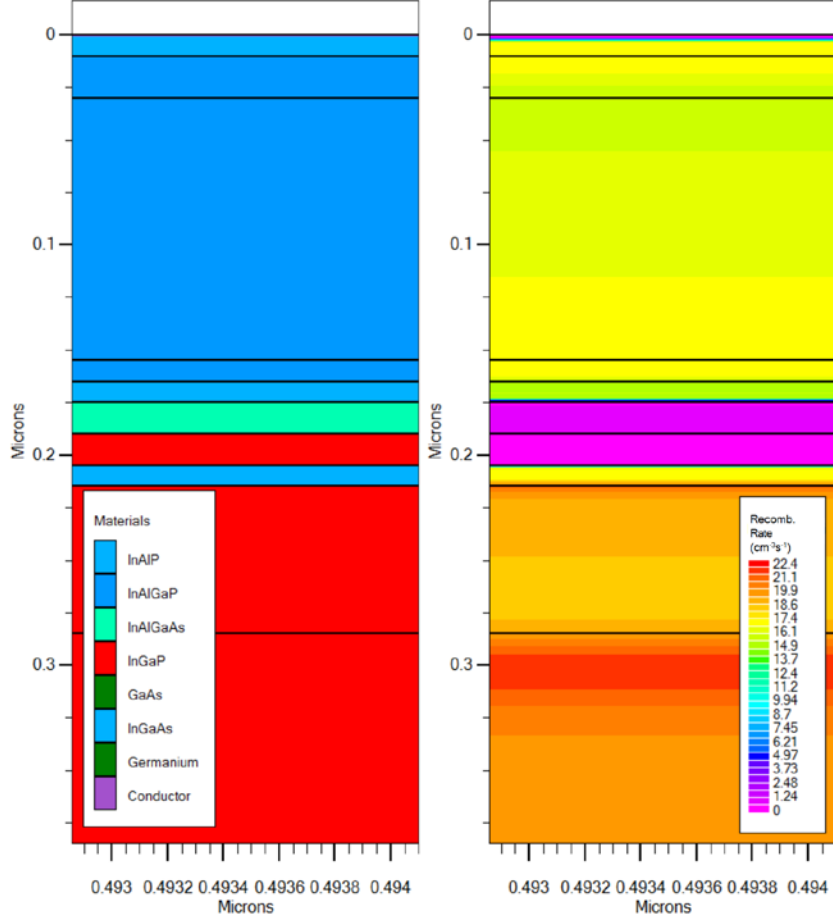


Figure 23. Baseline Cell Area of Highest Recombination Rate

B. OPTIMIZATION ITERATION NO. 1

The first round of optimization consisted of the following design space parameters: varying all window, buffer, and BSF layer thicknesses from $0.01 \mu\text{m}$ to $0.09 \mu\text{m}$ and doping concentrations from 10^{17} cm^{-3} to 10^{19} cm^{-3} ; varying all emitter and base layer thickness from $0.02 \mu\text{m}$ to $2.0 \mu\text{m}$ and doping concentrations from 10^{16} cm^{-3} to 10^{19} cm^{-3} . The number of simulation runs generated was 1024 using rotating and stacking. Simulation run time was approximately one day using a Linux machine with eight cores.

Distribution results for output power with and without outliers (outliers defined as output power less than 1.0 mW) are shown in Figure 24. The maximum output power achieved was 23.9297 mW with 755 runs failing to converge or giving faulty results. The mean without outliers was 9.2415 mW , and zero runs resulted in output power anywhere

near the baseline cell design. A sufficient linear regression model was unable to be fit to the data as all output power predictions were less than the baseline cell output power. To rectify the situation, the design space was required to be reduced over a more reasonable range.

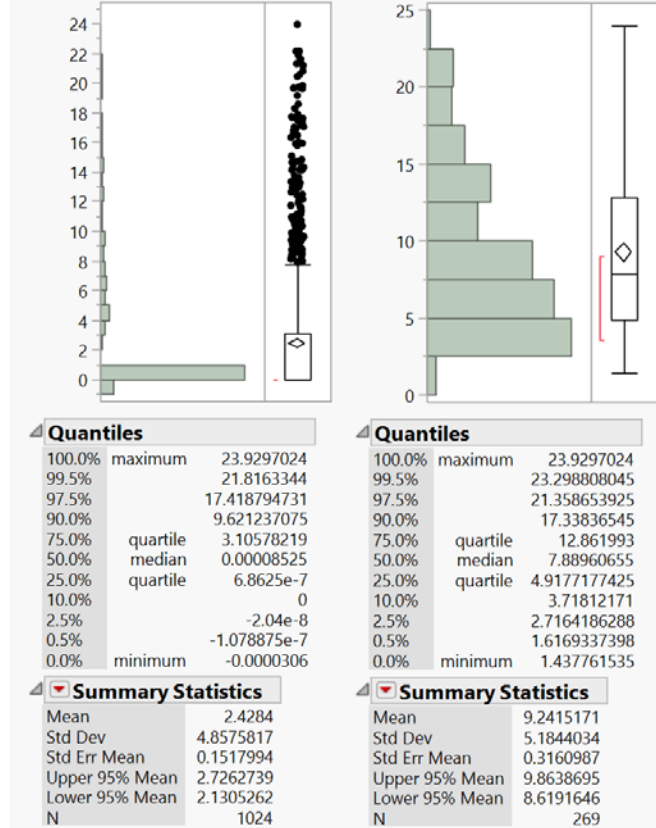


Figure 24. Iteration No. 1 Output Power Distributions with Outliers (left) and without Outliers (right)

C. OPTIMIZATION ITERATION NO. 2

In order to increase the number of successfully converged Silvaco ATLAS runs, the design space was re-centered around known successful results. The baseline cell served as the jumping off point. Choosing the design space was carried out via the following logic: if the baseline cell layer thickness was less than 0.5 μm , layer thickness was varied between 0.1 μm and 0.5 μm ; if the baseline cell layer thickness was greater than or equal to 0.5 μm , layer thickness was varied $\pm 20\%$; doping concentration

exponential component was varied $\pm 2.5\%$, as varying the doping concentration directly results in non-working cell layers. Additionally, the dynamic cell spacing was removed in favor of a set spacing guaranteed lower than the lowest thickness value. This ensured that sufficient spacing was available in the mesh at the p-n junctions while preventing too dense a mesh. Values for spacing were set at 5.0 nm for all window, emitter, buffer, and BSF layers and 50.0 nm for all base layers. The number of simulation runs generated were 1024 using rotating and stacking. Simulation run time was approximately one day using a Linux machine with eight cores.

Distribution results for the second iteration with and without outliers are shown in Figure 25. The maximum output power achieved was 44.8583 mW with 747 runs failing to converge or giving faulty results. The mean without outliers was 35.8597 mW, a value higher than the baseline cell's output power of 35.7907 mW. A stepwise linear regression model was able to be fit to the data.

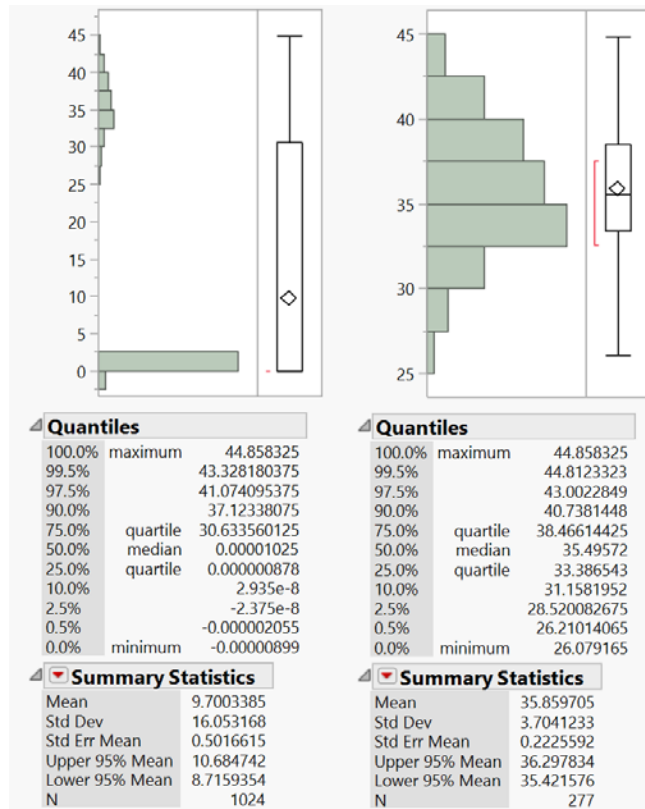


Figure 25. Iteration No. 2 Output Power Distributions with and without Outliers

The top ten most influential design parameters and relationships are shown in Table 4. From the model, the second cell parameters were the most influential based on their variance with extremely low p-values (1.905×10^{-98} for second cell BSF doping concentration). Smaller p-values indicate strong significance in the model.

Table 4. Iteration No. 2 Most Important Design Parameters and Relationships

Source	LogWorth	PValue
secbsfdopconc	97.720	0.00000
secbuffdopconc	97.314	0.00000
secbuffthick	92.918	0.00000
secwinthick	82.589	0.00000
topwinthick	81.901	0.00000
secbuffthick*secbuffdopconc	80.075	0.00000
secbsfdopconc*secbuffthick	78.738	0.00000
secbsfdopconc*secbsfdopconc	78.121	0.00000
secbasethick	78.035	0.00000
secbuffdopconc*secbuffdopconc	77.095	0.00000

A summary of the model fit is shown in Table 5. The R^2 value indicates how close the model is to fitting the linear regression line, with higher values being preferred and a value of 1.0 being the maximum.

Table 5. Iteration No. 2 Linear Regression Model Fit

Summary of Fit	
RSquare	1
RSquare Adj	1
Root Mean Square Error	0.000023
Mean of Response	35.85971
Observations (or Sum Wgts)	277

With a good fit model in place, the Profiler function in JMP was used. The Profiler allows JMP to project based on the fit model which values of the input factors result in the highest output power. The user can locate feasible peaks for layer thickness and doping concentration. A snapshot of the profiler is shown in Figure 26.

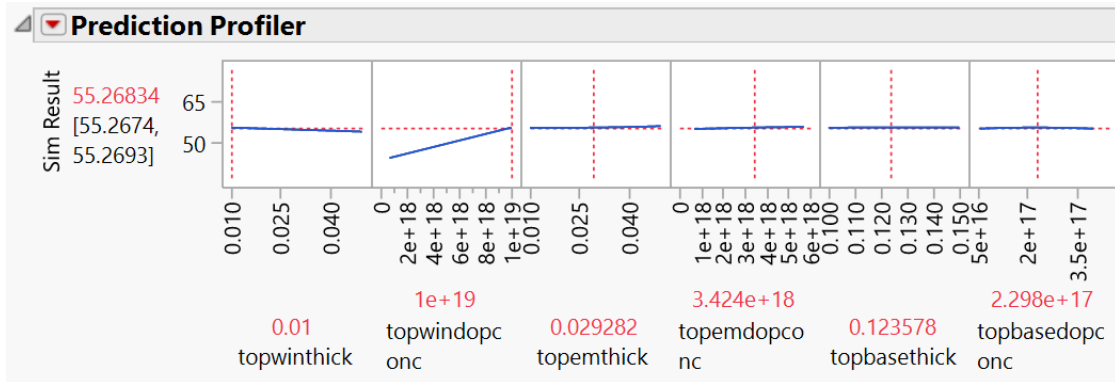


Figure 26. Using the Profiler for Predicting Optimum Input Factor Values

Although the model was a good fit and predicted high output power, one more optimization iteration was performed with one parameter changed to determine if a larger number of runs would converge and give a better model.

D. OPTIMIZATION ITERATION NO. 3

With the second cell buffer thickness being seen as statistically important for output power, and its baseline value being much higher than every non-emitter and non-base value (0.1 μ m), Optimization Iteration No. 3 sought to limit the design space to that of every other low thickness layer: 0.01 μ m to 0.05 μ m. The goal of this iteration was to determine if a better model could be established with a larger number of simulation convergences. All other design space bounds were kept the same as Optimization Iteration No. 2. Again, 1024 simulation runs were established and conducted. The iteration took approximately one day.

Distribution results for simulation output power with and without outliers is shown in Figure 27. The mean without outliers is slightly lower than the output power mean from Optimization Iteration No. 2 (33.5859 mW for No. 3, 35.8957 mW for No. 2) and the maximum power achieved for the design run is smaller (40.3607 mW for No. 3, 44.8583 mW for no. 2), but the number of successfully converged simulation runs is far greater for Optimization Iteration No. 3 comparatively (928 successful runs for No. 3, 277 successful runs for No. 2). The fit model was then examined.

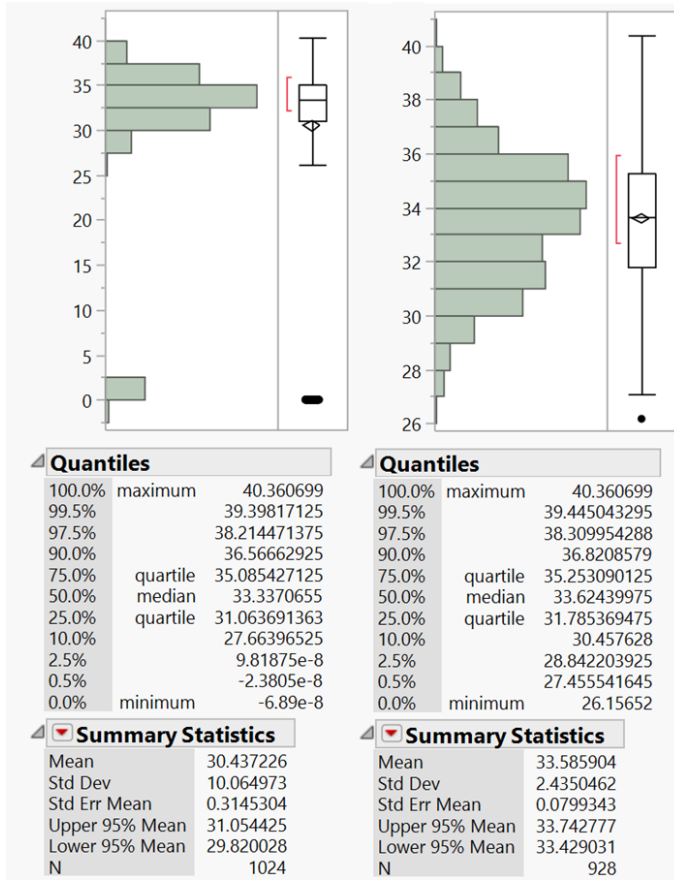


Figure 27. Iteration No. 3 Output Power Distributions with and without Outliers

The Summary of Fit for Optimization Iteration No. 3's stepwise linear regression model is shown in Table 6. The fit has a lower R^2 value than that of Optimization Iteration No. 2, and not all of the input factors could successfully be fit (28 input factors were successful, and 17 were unsuccessful). Additionally, when running the profiler and attempting to maximize output power, the confidence interval began to widen. The effect is shown in Figure 28. Lastly, the highest output power predicted when manipulating the profiler was far lower than that of Optimization Iteration No. 2 (55.0-mW range for No. 3 with a large confidence interval, greater than 60.0-mW range for No. 2 with small confidence interval). For this reason, Optimization Iteration No. 2's stepwise linear regression model was used for finding optimum input factors.

Table 6. Iteration No. 3 Linear Regression Model Fit

Summary of Fit	
RSquare	0.965427
RSquare Adj	0.96282
Root Mean Square Error	0.46953
Mean of Response	33.5859
Observations (or Sum Wgts)	928

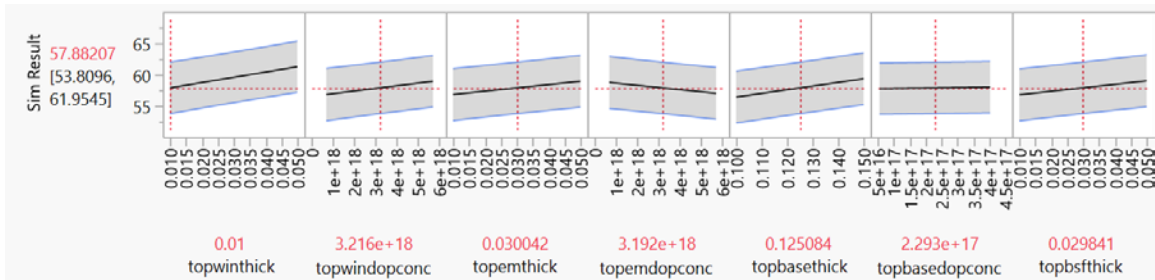


Figure 28. Iteration No. 3 Profiler with Widening Confidence Intervals

E. OPTIMIZED CELL RESULTS FROM ITERATION NO. 2 MODEL

The optimal cell configuration shown in Figure 29 was found using the JMP Profiler functions for the Optimization Iteration No. 2 stepwise linear regression model. Sim Result output power was predicted to be greater than 80.0 mW. Although this value was not believed to be achievable via actual simulation, the belief was that sufficiently large output power could still be achieved compared to baseline results. Notable changes in the optimized multi-junction cell included larger doping concentrations in the second cell BSF and buffer layers ($1.835 \times 10^{19} \text{ cm}^{-3}$ and $1.3 \times 10^{18} \text{ cm}^{-3}$, respectively) compared to the second cell BSF and buffer layers in the baseline multi-junction cell ($2.0 \times 10^{18} \text{ cm}^{-3}$ and $1.0 \times 10^{17} \text{ cm}^{-3}$, respectively). Varying the two concentrations by an order of magnitude was predicted to have the largest effect on output power compared to all other changes determined by the profiler.

Cathode			
Window	n+	0.01 μm	1E19 cm^{-3}
Emitter	n+	0.029282 μm	3.424E18 cm^{-3}
Base	p+	0.123578 μm	2.298E17 cm^{-3}
BSF	p+	0.03 μm	7.2E17 cm^{-3}
Buffer	p+	0.048 μm	1.582E18 cm^{-3}
Emitter	p+	0.015 μm	8E18 cm^{-3}
Base	n+	0.015 μm	1E19 cm^{-3}
Window	n+	0.01 μm	3.151E18 cm^{-3}
Emitter	n+	0.07 μm	3.284E18 cm^{-3}
Base	p+	0.5 μm	2.194E17 cm^{-3}
BSF	p+	0.03 μm	1.835E19 cm^{-3}
Buffer	p+	0.104 μm	1.3E18 cm^{-3}
Emitter	p+	0.015 μm	8E18 cm^{-3}
Base	n+	0.015 μm	1E19 cm^{-3}
Window	n+	0.028762 μm	3.231E18 cm^{-3}
Emitter	n+	0.028542 μm	3.186E18 cm^{-3}
Base	p+	0.26478 μm	2.293E17 cm^{-3}
BSF	p+	0.03 μm	3.197E18 cm^{-3}
Buffer	p+	0.028394 μm	1.541E18 cm^{-3}
Emitter	p+	0.015 μm	8E18 cm^{-3}
Base	n+	0.015 μm	1E19 cm^{-3}
Window	n+	0.03 μm	3.276E18 cm^{-3}
Emitter	n+	0.05 μm	3.141E18 cm^{-3}
Base	p+	1.3675 μm	1.812E17 cm^{-3}
BSF	p+	0.031271 μm	3.5E18 cm^{-3}
Buffer	p+	0.03 μm	1.636E18 cm^{-3}
Emitter	p+	0.015 μm	8E18 cm^{-3}
Base	n+	0.015 μm	1E19 cm^{-3}
Window	n+	0.028993 μm	3.182E18 cm^{-3}
Emitter	n+	0.030686 μm	7.06E17 cm^{-3}
Substrate	p+	149.96 μm	4.03E17 cm^{-3}
Anode			

Figure 29. Optimized 5-J Cell Based on Iteration No. 2 Model

The simulation results for the optimized cell, the baseline results for comparison, and percent change are shown in Table 7. Each factor increased somewhat, with

maximum output power increasing greater than 15.0 mW and FF rising to over 90%. The increased maximum output power gives a new efficiency of 37.3682%, a greater than 40% increase in efficiency.

Table 7. Silvaco ATLAS Optimized Cell Results and Comparison

Parameter	Baseline Cell	Optimized Cell	% Change
J_{sc}	9.80609 mA/cm ²	10.6448 mA/cm ²	+8.55%
V_{oc}	5.26026 V	5.31403 V	+1.022%
P_{max}	35.7907 mW	51.0147 mW	+42.436%
FF	69.3852%	90.1849%	+29.98%
Efficiency	26.2166%	37.3682%	+42.536%

The IV curve for the optimized 5-J cell is shown in Figure 30. The increased FF in Figure 30 is immediately noticeable compared to the baseline IV characteristic curve of Figure 19. The curve exhibits more of a box shape compared to the baseline's IV characteristic curve. Additionally, the slope of the top part of the curve in Figure 30 is nearly constant from the short-circuit current position until nearly 5.0 V is seen at the anode. The optimized cell's output power versus voltage is shown in Figure 31.

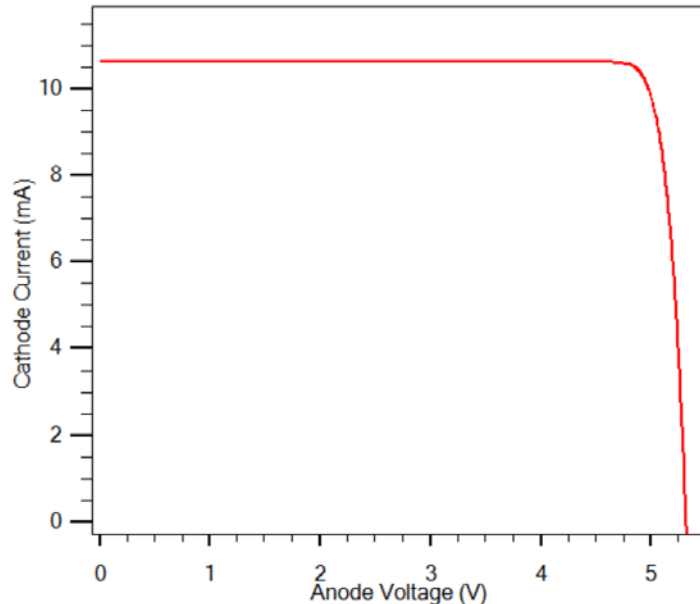


Figure 30. Optimized Cell IV Characteristic Curve

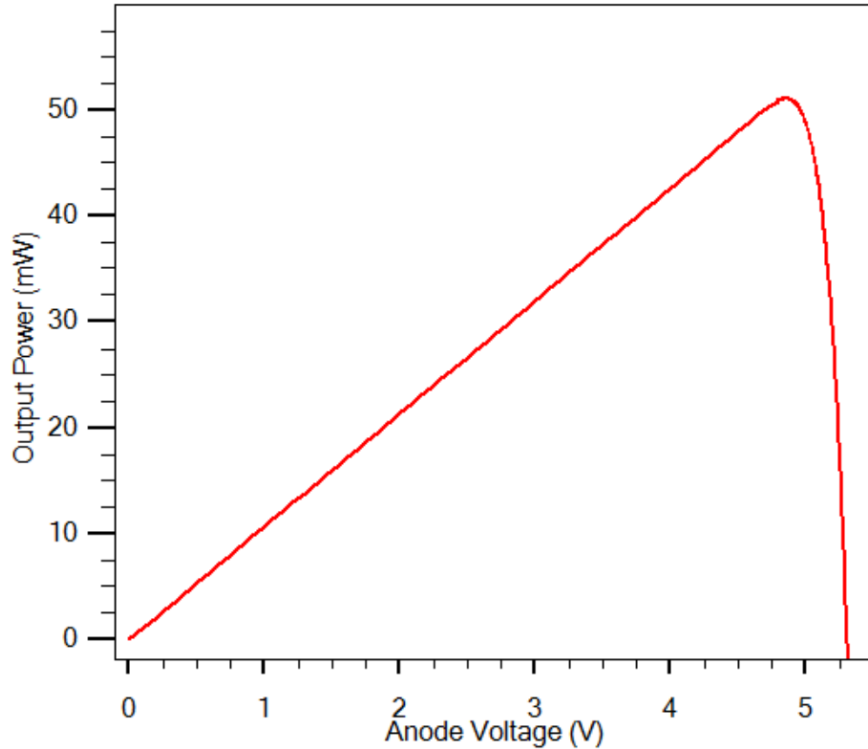


Figure 31. Optimized Cell Power versus Voltage

EQE for the optimized cell is shown in Figure 32. The second cell EQE increased nearly 20% due to the change in doping concentrations for the second cell buffer and BSF. The change in doping concentration in the second cell BSF acted to direct more minority carriers back toward the p-n junction to increase I_{sc} , while the increased doping concentration in the buffer acted to negate the electric field that prevented carrier flow across the tunnel junction. The third and fourth cells' EQE increased 8-10% compared to the baseline cell but still remained very small due to the tails in EQE for the first two cells. Cell 5 EQE decreased approximately 4-5% due to the higher utilization in the first four junctions and due to the tails shown by the other layers in Figure 31. The shape of each EQE curve in the optimized multi-junction cell remained relatively the same compared to the EQE curve shapes in the baseline multi-junction cell.

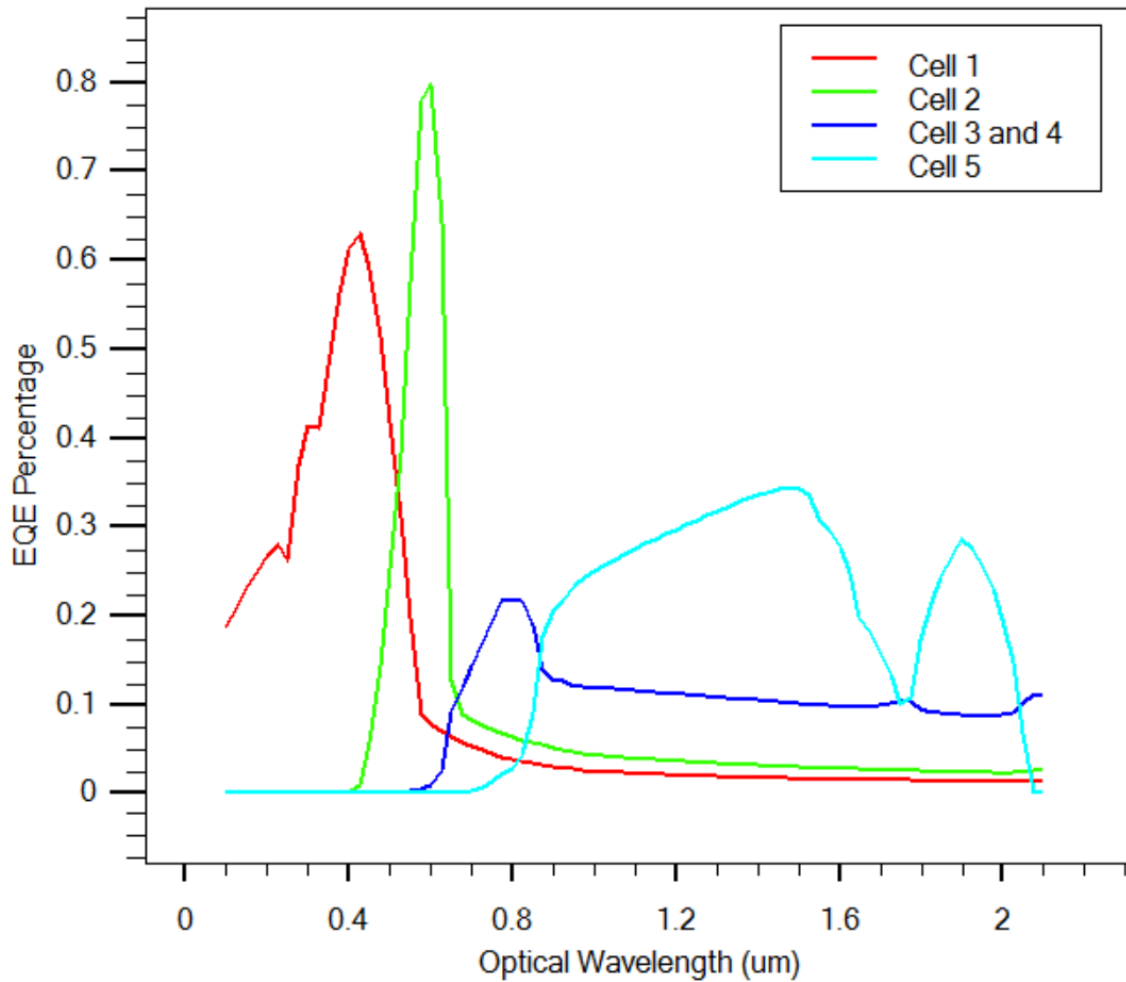


Figure 32. Optimized Cell EQE

The electric fields generated for the top three microns are shown on a logarithmic scale in Figure 33. The effect of the increased doping concentration for the second cell BSF and buffer layers can be seen in the second cell base with a much higher electric field concentration at the p-n junction compared to the baseline cell electric fields. The area of the second cell base's electric field also increased significantly compared to the baseline multi-junction cell. The third and fourth cell electric field concentrations and areas did not change significantly compared to the baseline multi-junction cell.

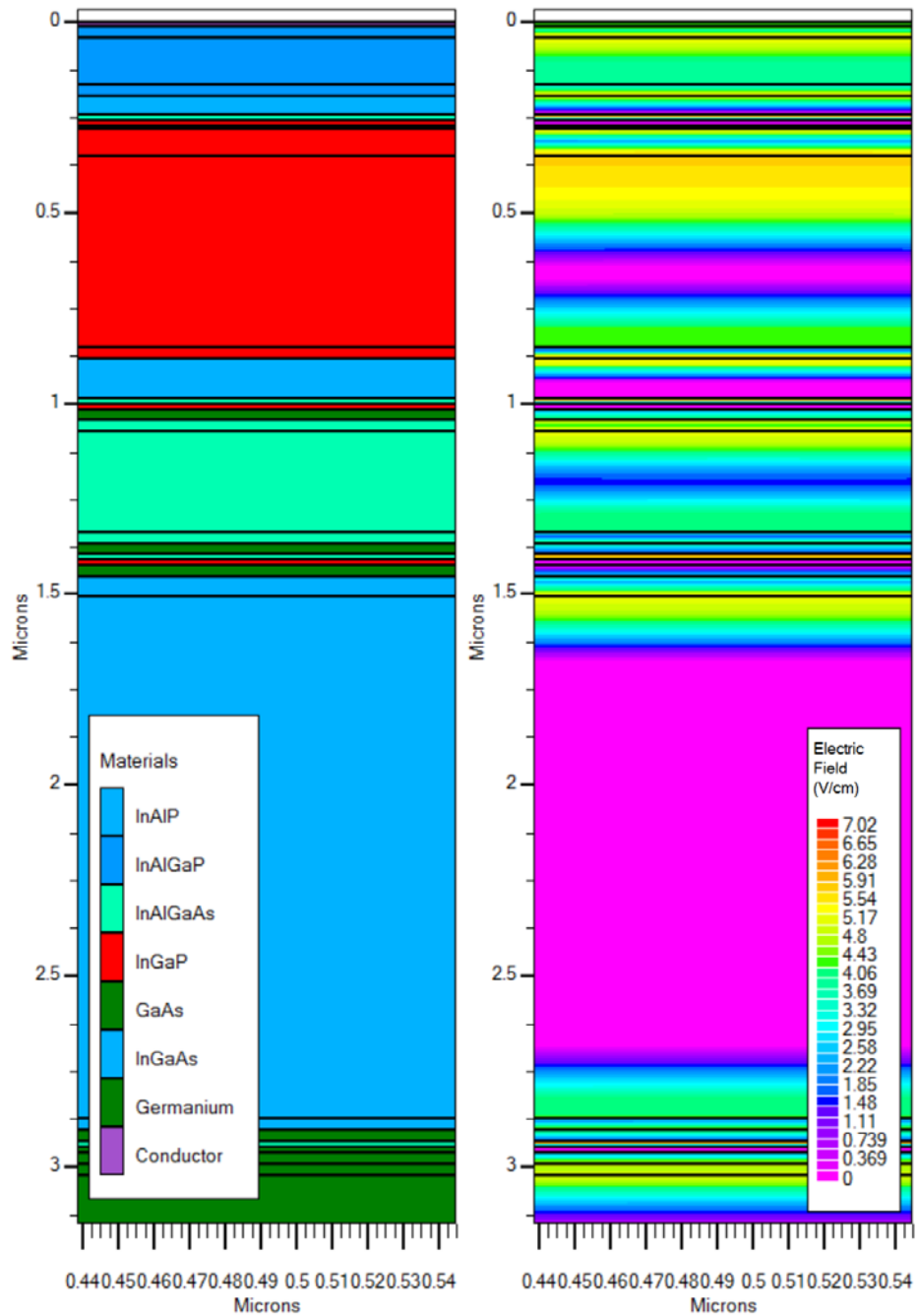


Figure 33. Electric Fields in Optimized Cell

The areas of highest recombination rate for the optimized cell are shown in Figure 34. Compared to the baseline cell, we experienced much more recombination in the first cell at the p-n junction between the emitter and base and less recombination in at the second cell base-emitter p-n junction. Almost the entire first cell base area had a

recombination rate of around $15 \text{ cm}^{-3}\text{s}^{-1}$, whereas for the optimized cell, the recombination rate was $18 \text{ cm}^{-3}\text{s}^{-1}$ or above. As the top two cells are the current limiting factors typically in multi-junction cells, this gives credence to the second cell being the current limiting component since despite the increased recombination in the top cell, efficiency was increased compared to the baseline.

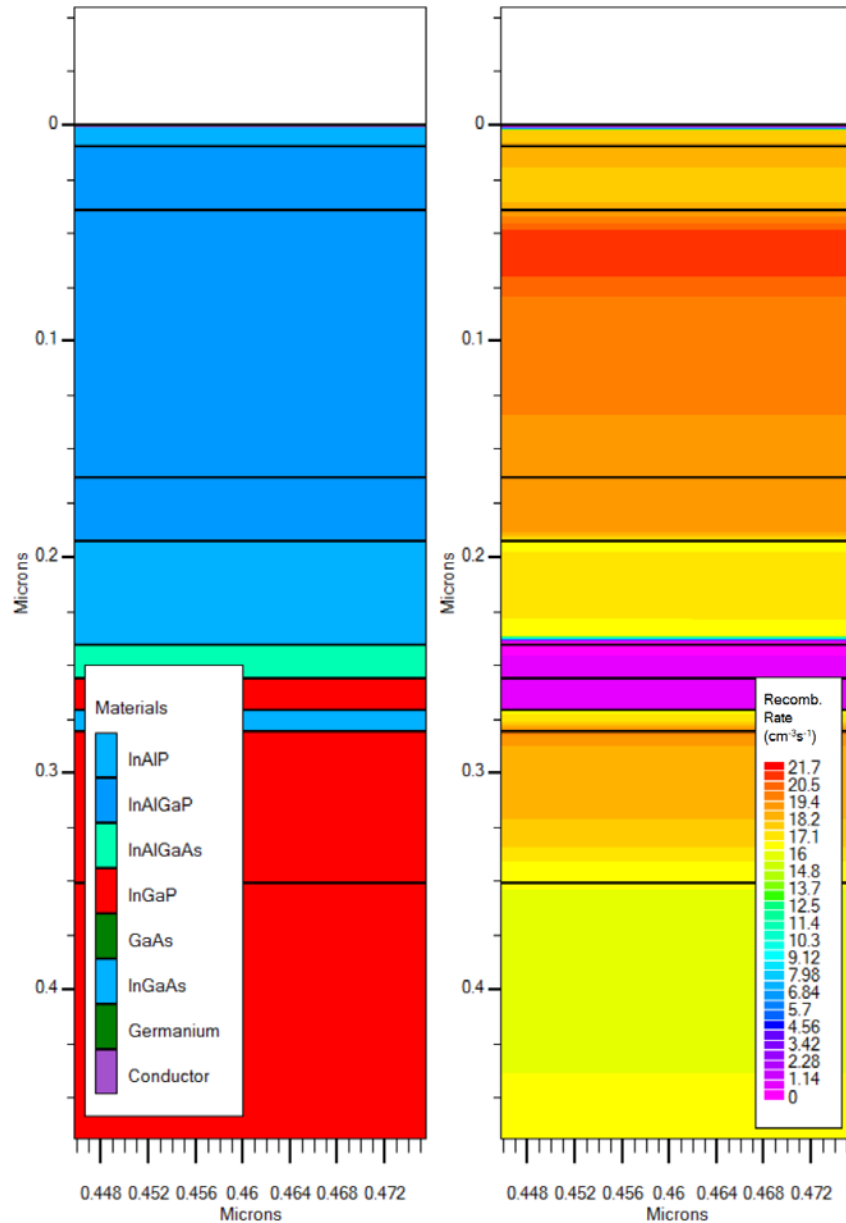


Figure 34. Optimized Cell Area of Highest Recombination Rate

THIS PAGE INTENTIONALLY LEFT BLANK

V. CONCLUSIONS AND FUTURE WORK

A. CONCLUSIONS

A five-junction solar cell was successfully modeled in Silvaco ATLAS using design specifications from a five-junction cell available in industry. This is significant in that few Silvaco ATLAS models with more than three junctions have been publicly researched or are readily available. Initial doping concentrations and layer thicknesses were established such that values for open-circuit voltage, short-circuit current, maximum power, fill factor, and efficiency were within reason to the Dimroth cell on which the model was based. Once the baseline cell was established with material properties gathered for each of the different cell layers, the simulation was successfully conducted. NOB DoE selection for the input factor design space was conducted over three optimization iterations with 1024 runs each to predict an optimized design given the 45 input factors. The optimized cell resulted in increased overall EQE, maximum output power greater than 50 mW, short circuit current greater than 10 mA, open circuit voltage greater than 5.3 V, fill factor greater than 90%, and efficiency greater than 36%. The most significant factors for the multi-junction cell based on the chosen materials proved to be the second cell buffer and BSF parameters. The modified factors shifted the area of highest recombination from the second cell to the first cell, resulting in higher current density overall due to the decreased recombination in the second cell outweighing the increased recombination in the first cell.

The method of optimization proved successful with some caveats. The initial design space proved too large for only 1024 simulations, leading to less than 300 successful run convergences. Following obtaining the final results, we discovered that more runs successfully converged when using 128-bit precision. Two of the unsuccessful runs for Optimization Iteration No. 2 were simulated a second time using 128-bit precision and successfully converged, albeit with output power lower than the optimized cell in those two cases. The failure to converge in most instances involved the beam statement being lowered to such a tiny amount that it never converged given the number of bits assigned. As the initial baseline design was done on a Windows machine and not

Linux, the usage of 128-bit processing in Silvaco ATLAS to solve the convergence issue was unknown until late in the research.

B. FUTURE WORK

1. Conduct Optimization with 128-bit Precision and More Design Runs

The initial design space resulted in a poor linear regression model due to the limited number of successful runs and maximum output power being far less than the baseline cell values. Conducting Optimization Iteration No. 1 with 128-bit precision and more instances of rotating and stacking to make a denser design space would most likely lead to a more robust stepwise linear regression model. Whole sections of the available design space were not simulated and may likely lead to a more optimized design than what was discovered during this research.

2. Refractive Index Files

Much of the lower EQE in the third, fourth, and fifth junctions suffered from extinction coefficients existing beneath the bandgap. Simulation with different refractive index data than that provided by the SOPRA database would rectify the observed anomaly and raise the EQE for the lower-level junctions. This will become increasingly more difficult as the exotic nature of the specified ternary or quaternary increases.

3. Physical Tunnel Junctions

The workaround of using an electrode across the tunnel junction regions allowed for exploring the phenomena in the cell regions themselves but did not offer accurate quantum tunneling. The effects occurring in the tunnel junction regions was one of the chief losses of efficiency in the Dimroth et al. design [9]. A five-junction cell simulation with tunnel junctions that appropriately modeled quantum tunneling for more than one tunnel region would vastly enhance the model's validity and application for designing multi-junction cells.

4. Material Variance in Design

The Dimroth design was built as a radiation-resistant multi-junction cell and not for the highest efficiency. Changing materials via mole fractions for each of the different cell layers would lead to different variable relationships than those discovered during this research. Additionally, a high-efficiency three or four-junction design with an added layer appropriate for the given bandwidths could be explored to obtain theoretical efficiency greater than 40%.

5. Parallel Processing via a Supercomputer

The Hamming supercomputer at NPS was unfortunately unavailable for use in running parallel Silvaco ATLAS simulations during this research. Being able to run 30 or more simulations at once that did not rely on one another for inputs would vastly decrease the time required for simulation and speed up the design process as a result.

6. Physical Fabrication of Multi-junction Cell Design

Although this would potentially be cost-prohibitive depending on availability of a process line, physically constructing and utilizing the optimized cell design in the real world would lend validity to the simulation results and further solidify the optimization and modeling techniques in this research as valid methods for multi-junction solar cell design.

7. Alternative Designs Explored

Five-junction solar cell designs with different material layer makeups and properties than the Fraunhofer ISE cell can be integrated into the input deck used in this thesis and optimized in a similar fashion. Cells with different defining characteristics than the radiation-hardened Fraunhofer ISE cell can be explored and simulated.

8. Simulate with Different Air Mass Spectrums

The multi-junction cell in this thesis was optimized for the AM0 spectrum. Varying the air mass for terrestrial application will lead to a different relationship and importance correlation for the input factors than those found for the optimization in AM0.

THIS PAGE INTENTIONALLY LEFT BLANK

APPENDIX A. ATLAS BASELINE INPUT DECK

A. BASELINE SILVACO ATLAS INPUT DECK

```
#go atlas simflags="-P 8"
go atlas

set topwinthick= 0.01
set topwindopconc= 2E18
set topemthick= 0.02
set topemdopconc= 2E18
set topbasethick= 0.125
set topbasedopconc= 1.5E17
set topbsfthick= 0.01
set topbsfdopconc= 2E18
set topbuffthick= 0.01
set topbuffdopconc= 1E18
set secwinthick= 0.01
set secwindopconc= 2E18
set secemthick= 0.07
set secemdopconc= 2E18
set secbasethick= 0.5
set secbasedopconc= 1.5E17
set secbsfthick= 0.01
set secbsfdopconc= 2E18
set secbuffthick= 0.1
set secbuffdopconc= 1E17
set thirdwinthick= 0.03
set thirwindopconc= 2E18
set thirdemthick= 0.03
set thirdemdopconc= 2E18
set thirdbasethick= 0.275
set thirdbasedopconc= 1.5E17
set thirdbsfthick= 0.03
set thirdbsfopconc= 2E18
set thirdbuffthick= 0.03
set thirdbuffdopconc= 1E18
set fourthwinthick= 0.03
set fourthwindopconc= 2E18
set fourthemthick= 0.05
set fourthemdopconc= 2E18
set fourthbasethick= 0.965
set fourthbasedopconc= 1.5E17
set fourthbsfthick= 0.03
set fourthbsfdopconc= 2E18
set fourthbuffthick= 0.03
set fourthbuffdopconc= 1E18
set botwinthick= 0.03
set botwindopconc= 2E18
set botemthick= 0.01
set botemdopconc= 2E18
set botsubsthick= 149.96
set botsubsdopconc= 1.5E17

set topcellthick= $topwinthick+$topemthick+$topbasethick+$topbsfthick+$topbuffthick
set tunlemthick= 0.015
set tunlemdopconc= 8E18
set tunlbasethick= 0.015
set tunlbasedopconc= 1E19
set tunlthick= $tunlemthick+$tunlbasethick
set seccellthick= $secwinthick+$secemthick+$secbasethick+$secbsfthick+$secbuffthick
set toptwosections= $topcellthick+$tunlthick+$seccellthick
set tun2emthick= 0.015
set tun2emdopconc= 8E18
set tun2basethick= 0.015
set tun2basedopconc= 1E19
set tun2thick= $tun2emthick+$tun2basethick
set thirdcellthick= $thirdwinthick+$thirdemthick+$thirdbasethick+$thirdbsfthick+$thirdbuffthick
set topthreesections= $toptwosections+$tun2thick+$thirdcellthick
set tun3emthick= 0.015
set tun3emdopconc= 8E18
set tun3basethick= 0.015
set tun3basedopconc= 1E18
set tun3thick= $tun3emthick+$tun3basethick
```

```

set fourthcellthick= $fourthwinthick+$fourthemthick+$fourthbasethick+$fourthbsfthick+$fourthbuffthick
set topfoursections= $topthreesections+$tun3thick+$fourthcellthick
set tun4emthick= 0.015
set tun4emdopconc= 8E18
set tun4basethick= 0.015
set tun4basedopconc= 1E19
set tun4thick= $tun4emthick+$tun4basethick
set botcellthick= $botwinthick+$botemthick+$botsubsthick
set fullmjcellthick= $topfoursections+$tun4thick+$botcellthick
#####
#Meshes
#####
#mesh auto
mesh width= 1 space.mult=1
x.m loc=0.0 s=0.25
#x.m loc=0.49 s=0.02
#x.m loc=0.51 s=0.02
x.m loc=1.0 s=0.25

# Top Cell
y.mesh loc=0.0 spac=0.003
# Window
y.mesh loc=$topwinthick spac=0.3*$topwinthick
# Emitter
y.mesh loc=$topwinthick+$topemthick spac=0.15*$topemthick
# Base
y.mesh loc=$topwinthick+$topemthick+$topbasethick spac=0.2*$topbasethick
# BSF
y.mesh loc=$topwinthick+$topemthick+$topbasethick+$topbsfthick spac=0.3*$topbsfthick
# Buffer
y.mesh loc=$topcellthick spac=0.2*$topbuffthick

# Tunnel 1
# Tunnel Emitter
y.mesh loc=$topcellthick+$tun1emthick spac=0.001
# Tunnel Base
y.mesh loc=$topcellthick+$tun1thick spac=0.001

# Second Cell
# Window
y.mesh loc=$topcellthick+$tun1thick+$secwinthick spac=0.3*$secwinthick
# Emitter
y.mesh loc=$topcellthick+$tun1thick+$secwinthick+$secemthick spac=0.04*$secemthick
# Base
y.mesh loc=$topcellthick+$tun1thick+$secwinthick+$secemthick+$secbasethick spac=0.06*$secbasethick
# BSF
y.mesh loc=$topcellthick+$tun1thick+$secwinthick+$secemthick+$secbasethick+$secbsfthick
spac=0.3*$secbsfthick
# Buffer
y.mesh loc=$toptwosections spac=0.02*$secbuffthick

# Tunnel 2
# Tunnel Emitter
y.mesh loc=$toptwosections+$tun2emthick spac=0.001
# Tunnel Base
y.mesh loc=$toptwosections+$tun2thick spac=0.001

# Third Cell
# Window
y.mesh loc=$toptwosections+$tun2thick+$thirdwinthick spac=0.1*$thirdwinthick
# Emitter
y.mesh loc=$toptwosections+$tun2thick+$thirdwinthick+$thirdemthick spac=0.1*$thirdemthick
# Base
y.mesh loc=$toptwosections+$tun2thick+$thirdwinthick+$thirdemthick+$thirdbasethick
spac=0.11*$thirdbasethick
# BSF
y.mesh loc=$toptwosections+$tun2thick+$thirdwinthick+$thirdemthick+$thirdbasethick+$thirdbsfthick
spac=0.1*$thirdbsfthick
# Buffer
y.mesh loc=$topthreesections spac=0.067*$thirdbuffthick

# Tunnel 3
# Tunnel Emitter
y.mesh loc=$topthreesections+$tun3emthick spac=0.001
# Tunnel Base
y.mesh loc=$topthreesections+$tun3thick spac=0.001

# Fourth Cell
# Window

```

```

y.mesh loc=$topthreesections+$tun3thick+$fourthwinthick spac=0.1*$fourthwinthick
# Emitter
y.mesh loc=$topthreesections+$tun3thick+$fourthwinthick+$fourthemthick spac=0.06*$fourthemthick
# Base
y.mesh loc=$topthreesections+$tun3thick+$fourthwinthick+$fourthemthick+$fourthbasethick
spac=0.03*$fourthbasethick
# BSF
y.mesh
loc=$topthreesections+$tun3thick+$fourthwinthick+$fourthemthick+$fourthbasethick+$fourthbsfthick
spac=0.1*$fourthbsfthick
# Buffer
y.mesh loc=$topfoursections spac=0.067*$fourthbuffthick

# Tunnel 4
# Tunnel Emitter
y.mesh loc=$topfoursections+$tun4emthick spac=0.001
# Tunnel Base
y.mesh loc=$topfoursections+$tun4thick spac=0.001

# Bottom Cell
# Window
y.mesh loc=$topfoursections+$tun4thick+$botwinthick spac=0.1*$botwinthick
# Emitter
y.mesh loc=$topfoursections+$tun4thick+$botwinthick+$botemthick spac=0.3*$botemthick
# Substrate
y.mesh loc=$fullmjcellthick spac=50

#####
#Regions
#####
#top cell
region num=1 name="n+ type AlInP" material=AlInP y.min=0.0 y.max=$topwinthick
region num=2 name="n+ type AlGaInP" material=AlGaInP y.min=$topwinthick y.max=$topwinthick+$topemthick
x.comp=0.3
region num=3 name="p+ type AlGaInP" material=AlGaInP y.min=$topwinthick+$topemthick
y.max=$topwinthick+$topemthick+$topbasethick x.comp=0.3
region num=4 name="p+ type AlGaInP" material=AlGaInP y.min=$topwinthick+$topemthick+$topbasethick \
y.max=$topwinthick+$topemthick+$topbasethick+$topbsfthick x.comp=0.3
region num=5 name="p+ type AlInP" material=AlInP
y.min=$topwinthick+$topemthick+$topbasethick+$topbsfthick \
y.max=$topcellthick

#tunnel 1
region num=6 name="p+ type AlGaInAs" material=AlGaInAs y.min=$topcellthick
y.max=$topcellthick+$tunlemthick
region num=7 name="n+ type GaInP" material=GaInP y.min=$topcellthick+$tunlemthick
y.max=$topcellthick+$tunlthick

#second cell
region num=8 name="n+ type AlInP" material=AlInP y.min=$topcellthick+$tunlthick
y.max=$topcellthick+$tunlthick+$secwinthick
region num=9 name="n+ type GaInP" material=GaInP y.min=$topcellthick+$tunlthick+$secwinthick \
y.max=$topcellthick+$tunlthick+$secwinthick+$secemthick
region num=10 name="p+ type GaInP" material=GaInP
y.min=$topcellthick+$tunlthick+$secwinthick+$secemthick \
y.max=$topcellthick+$tunlthick+$secwinthick+$secemthick+$secbasethick
region num=11 name="p+ type GaInP" material=GaInP
y.min=$topcellthick+$tunlthick+$secwinthick+$secemthick+$secbasethick \
y.max=$topcellthick+$tunlthick+$secwinthick+$secemthick+$secbasethick+$secbsfthick
region num=12 name="p+ type AlInP" material=AlInP
y.min=$topcellthick+$tunlthick+$secwinthick+$secemthick+$secbasethick+$secbsfthick \
y.max=$toptwosections

#tunnel 2
region num=13 name="p+ type AlGaInAs" material=AlGaInAs y.min=$toptwosections
y.max=$toptwosections+$tun2emthick
region num=14 name="n+ type GaInP" material=GaInP y.min=$toptwosections+$tun2emthick
y.max=$toptwosections+$tun2thick

#third cell
region num=15 name="n+ type GaAs" material=GaAs y.min=$toptwosections+$tun2thick
y.max=$toptwosections+$tun2thick+$thirdwinthick
region num=16 name="n+ type AlGaInAs" material=AlGaInAs
y.min=$toptwosections+$tun2thick+$thirdwinthick \
y.max=$toptwosections+$tun2thick+$thirdwinthick+$thirdemthick
region num=17 name="p+ type AlGaInAs" material=AlGaInAs
y.min=$toptwosections+$tun2thick+$thirdwinthick+$thirdemthick \
y.max=$toptwosections+$tun2thick+$thirdwinthick+$thirdbasethick

```

```

region num=18 name="p+ type AlGaInAs" material=AlGaInAs
y.min=$toptwosections+$tun2thick+$thirdwinthick+$thirdemthick+$thirdbasethick \
y.max=$toptwosections+$tun2thick+$thirdwinthick+$thirdemthick+$thirdbasethick+$thirdbsfthick
region num=19 name="p+ type GaAs" material=GaAs
y.min=$toptwosections+$tun2thick+$thirdwinthick+$thirdemthick+$thirdbasethick+$thirdbsfthick \
y.max=$topthreesections
#tunnel 3
region num=20 name="p+ type AlGaInAs" material=AlGaInAs      y.min=$topthreesections
y.max=$topthreesections+$tun3emthick
region num=21 name="n+ type GaInP" material=GaInP  y.min=$topthreesections+$tun3emthick
y.max=$topthreesections+$tun3thick

#fourth cell
region num=22 name="n+ type GaAs" material=GaAs y.min=$topthreesections+$tun3thick
y.max=$topthreesections+$tun3thick+$fourthwinthick
region num=23 name="n+ type InGaAs" material=InGaAs y.min=$topthreesections+$tun3thick+$fourthwinthick \
y.max=$topthreesections+$tun3thick+$fourthwinthick+$fourthemthick x.comp=0.01
region num=24 name="p+ type InGaAs" material=InGaAs
y.min=$topthreesections+$tun3thick+$fourthwinthick+$fourthemthick \
y.max=$topthreesections+$tun3thick+$fourthwinthick+$fourthemthick+$fourthbasethick x.comp=0.01
region num=25 name="p+ type InGaAs" material=InGaAs
y.min=$topthreesections+$tun3thick+$fourthwinthick+$fourthemthick+$fourthbasethick \
y.max=$topthreesections+$tun3thick+$fourthwinthick+$fourthemthick+$fourthbasethick+$fourthbsfthick x.comp=0.01
region num=26 name="p+ type GaAs" material=GaAs
y.min=$topthreesections+$tun3thick+$fourthwinthick+$fourthemthick+$fourthbasethick+$fourthbsfthick \
y.max=$topfoursections

#tunnel 4
region num=27 name="p+ type AlGaInAs" material=AlGaInAs      y.min=$topfoursections
y.max=$topfoursections+$tun4emthick
region num=28 name="n+ type InGaAs" material=InGaAs y.min=$topfoursections+$tun4emthick
y.max=$topfoursections+$tun4thick

#bot cell
region num=29 name="n+ type GaAs" material=GaAs y.min=$topfoursections+$tun4thick
y.max=$topfoursections+$tun4thick+$botwinthick
region num=30 name="n+ type Ge" material=Ge y.min=$topfoursections+$tun4thick+$botwinthick
y.max=$topfoursections+$tun4thick+$botwinthick+$botemthick
region num=31 name="p+ type Ge" material=Ge y.min=$topfoursections+$tun4thick+$botwinthick+$botemthick
y.max=$fullmjcellthick

electrode num=1 name=cathode top
electrode num=2 material=AlGaInAs name=tunnel1top y.min=$topcellthick y.max=$topcellthick+$tun1emthick
electrode num=3 material=GaInP name=tunnel1bot y.min=$topcellthick+$tun1emthick
y.max=$topcellthick+$tun1thick
electrode num=4 material=AlGaInAs name=tunnel2top y.min=$toptwosections
y.max=$toptwosections+$tun2emthick
electrode num=5 material=GaInP name=tunnel2bot y.min=$toptwosections+$tun2emthick
y.max=$toptwosections+$tun2thick
electrode num=6 material=AlGaInAs name=tunnel3top y.min=$topthreesections
y.max=$topthreesections+$tun3emthick
electrode num=7 material=GaInP name=tunnel3bot y.min=$topthreesections+$tun3emthick
y.max=$topthreesections+$tun3thick
electrode num=8 material=AlGaInAs name=tunnel4top y.min=$topfoursections
y.max=$topfoursections+$tun4emthick
electrode num=9 material=GaAs name=tunnel4bot y.min=$topfoursections+$tun4emthick
y.max=$topfoursections+$tun4thick
electrode num=10 name=anode bot

contact name=tunnel1top resist=0.125E17
contact name=tunnel1bot resist=0.125E17
contact name=tunnel2top resist=0.125E17
contact name=tunnel2bot resist=0.125E17
contact name=tunnel3top resist=0.125E17
contact name=tunnel3bot resist=0.125E17
contact name=tunnel4top resist=0.125E17
contact name=tunnel4bot resist=0.125E17

#####
# DOPING - n-emitter on p-base
#####
# Top Cell
# Window
doping uniform region=1 n.type conc=$topwindopconc
# Emitter

```

```

doping uniform region=2 n.type conc=$topemdopconc
# Base
doping uniform region=3 p.type conc=$topbasedopconc
# BSF
doping uniform region=4 p.type conc=$topbsfdopconc
# Buffer
doping uniform region=5 p.type conc=$topbuffdopconc

# Tunnel 1
# Tunnel Emitter
doping uniform region=6 p.type conc=$tunlemdopconc
# Tunnel Base
doping uniform region=7 n.type conc=$tunlbasedopconc

# Second Cell
# Window
doping uniform region=8 n.type conc=$secwindopconc
# Emitter
doping uniform region=9 n.type conc=$secemdopconc
# Base
doping uniform region=10 p.type conc=$secbasedopconc
# BSF
doping uniform region=11 p.type conc=$secbsfdopconc
# Buffer
doping uniform region=12 p.type conc=$secbuffdopconc

# Tunnel 2
# Tunnel Emitter
doping uniform region=13 p.type conc=$tun2emdopconc
# Tunnel Base
doping uniform region=14 n.type conc=$tun2basedopconc

# Third Cell
# Window
doping uniform region=15 n.type conc=$thirdwindopconc
# Emitter
doping uniform region=16 n.type conc=$thirdemdopconc
# Base
doping uniform region=17 p.type conc=$thirdbasedopconc
# BSF
doping uniform region=18 p.type conc=$thirdbbsfdopconc
# Buffer
doping uniform region=19 p.type conc=$thirdbuffdopconc

# Tunnel 3
# Tunnel Emitter
doping uniform region=20 p.type conc=$tun3emdopconc
# Tunnel Base
doping uniform region=21 n.type conc=$tun3basedopconc

# Fourth Cell
# Window
doping uniform region=22 n.type conc=$fourthwindopconc
# Emitter
doping uniform region=23 n.type conc=$fourthemdopconc
# Base
doping uniform region=24 p.type conc=$fourthbasedopconc
# BSF
doping uniform region=25 p.type conc=$fourthbsfdopconc
# Buffer
doping uniform region=26 p.type conc=$fourthbuffdopconc

# Tunnel 4
# Tunnel Emitter
doping uniform region=27 p.type conc=$tun3emdopconc
# Tunnel Base
doping uniform region=28 n.type conc=$tun3basedopconc

# Window
doping uniform region=29 n.type conc=$botwindopconc
# Emitter
doping uniform region=30 n.type conc=$botemdopconc
# Substrate
doping uniform region=31 p.type conc=$botsubsdopconc

material material=AlGaInP sopra=Againp3_test_217.nk
#material material=AlGaInP sopra=Againp3.nk
#material material=AlInP sopra=Againp10_mod.nk
material material=AlInP sopra=Againp10.nk

```

```

material material=GaInP index.file=solarex03.nk
#material material=AlGaInAs sopra=Algaas1.nk
material material=AlGaInAs index.file=algaas_mod.nk
material material=InGaAs sopra=Ringas.all
material material=GaAs sopra=Gaas.nk
material material=Ge sopra=Ge.nk

#####
# MATERIAL PROPERTIES
#####

# AlInP
material material=AlInP EG300=2.4 PERMITTIVITY=11.7 AFFINITY=4.2
material material=AlInP MUN=2291 MUP=142
material material=AlInP NC300=1.08e20 NV300=1.28e19
material material=AlInP AUGN=5.447e-30 AUGP=2.957e-29 COPT=1e-10 TAUN=1e-06 TAUP=1e-06

# AlGaInP
material material=AlGaInP EG300=2.1744 PERMITTIVITY=12.16 AFFINITY=4.26
# Mich.
material material=AlGaInP MUN=1000 MUP=500
# Laserex05.in
material material=AlGaInP NC300=9.13e17 NV300=7.81E18
material material=AlGaInP taun0=1e-9 taup0=2e-8 copt=1.5e-10

# GaInP, O'Connor Dissert
material material=GaInP EG300=1.9 PERMITTIVITY=11.8 AFFINITY=4.09
# mobilities from Mich.
material material=GaInP MUN=1945 MUP=141
material material=GaInP NC300=6.55E17 NV300=1.5e19
material material=GaInP AUGN=3e-30 AUGP=3e-30 COPT=1e-10 TAUN=4e-09 TAUP=4e-09

# AlGaInAs
# various
material material=AlGaInAs EG300=1.51 PERMITTIVITY=12.8 AFFINITY=3.96
material material=AlGaInAs MUN=3000 MUP=150
material material=AlGaInAs NC300=6.54E17 NV300=1.12E19
material material=AlGaInAs AUGN=3e-30 AUGP=3e-30 COPT=1e-10 TAUN=1e-06 TAUP=1e-06

# InGaAs
material material=InGaAs EG300=1.41 PERMITTIVITY=13.12 AFFINITY=4.08
material material=InGaAs MUN=3000 MUP=150
material material=InGaAs NC300=3.93E17 NV300=9.1137E18
material material=InGaAs AUGN=3e-30 AUGP=3e-30 COPT=1e-10 TAUN=1E-09 TAUP=1E-09

# GaAs, O'Connor Dissert
material material=GaAs EG300=1.424 PERMITTIVITY=12.9 AFFINITY=4.07
# mobilities from Micho.
material material=GaAs MUN=8500 MUP=400
material material=GaAs NC300=4.7e17 NV300=9e18
material material=GaAs AUGN=1e-30 AUGP=1e-30 COPT=1e-11 TAUN=510E-9 TAUP=510E-9

# Ge, O'Connor Dissert
material material=Ge EG300=0.66 PERMITTIVITY=16.2 AFFINITY=4
# mobilities from Micho.
material material=Ge MUN=3900 MUP=1800
material material=Ge NC300=1.04e19 NV300=6e18
material material=Ge AUGN=1e-30 AUGP=1e-30 COPT=6.41E-14 TAUN=3.8E-3 TAUP=3.8E-3

models srh auger optr fermi conmob bgn temp=300 print
#bbt.nonlocal bbt.nlnderivs
#models srh temp=300 print

method newton itlimit=40 maxtraps=10 climit=1 dvmax=0.1
output con.band val.band

beam num=5 x.origin=0.5 y.origin=-5 angle=90 back.refl wavel.start=0.12 wavel.end=3 wavel.num=1500 AM0
solve init
solve b5=1e-01
solve b5=1

#save outf=top2sections.str
#tonyplot top2sections.str

log outf=dimroth.log

```

```

#save outf=dimroth.str
#tonyplot dimroth.str
solve previous
solve vanode=0.001
solve vanode=0.05
solve vstep=0.05 vfinal=4.8 name=anode
solve vanode=4.8 vstep=0.005 vfinal=5.3 name=anode

extract init infile="dimroth.log"
extract name="Isc" max(curve(v."anode," i."cathode"))
extract name="Jsc_mAcm2" $Isc*1e08*1e03
extract name="Voc" x.val from curve(v."anode," i."cathode") where y.val=0.0
extract name="Pm" max(curve(v."anode," (v."anode" * i."cathode")))
extract name="Pmax_mWcm2" $Pm*1e08*1e03
extract name="Vm" x.val from curve(v."anode," (v."anode" * i."cathode")) where y.val=$Pm
extract name="Im_mAcm2" $Vm*1e08*1e03
extract name="FF" ($Pm/($Isc*$Vm))*100
extract name="intens" max(bean."5")
extract name="Eff" (1e08*$Pm/$intens)*100
extract name="iv" curve(v."anode," i."cathode")*1e08*1e03) outfile="dimroth.dat"
#tonyplot dimroth.dat
#-set IV_set.set
Quit

```

B. EXAMPLE SILVACO ATLAS CODE FOR FINDING EQE FOR A CELL

```

# Mesh, region, doping, material property, and models statements all appear before this point
output con.band val.band band.temp opt.intensity

beam num=1 angle=90 x.origin=0.5 y.origin=-5 front.refl back.refl reflect=2
#beam num=2 angle=90 x.origin=0.5 y.origin=-5 wavelength=0.4 front.refl back.refl reflect=2
beam num=3 angle=90 x.origin=0.5 y.origin=-5 wavelength=0.57 front.refl back.refl reflect=2
beam num=4 angle=90 x.origin=0.5 y.origin=-5 wavelength=0.68 front.refl back.refl reflect=2
beam num=5 angle=90 x.origin=0.5 y.origin=-5 wavelength=0.86 front.refl back.refl reflect=2
beam num=6 angle=90 x.origin=0.5 y.origin=-5 wavelength=1.55 front.refl back.refl reflect=2

# Part 1:
solve init
log outf=tmp.log
solve b3=2 b4=2 b5=2 b6=2
extract init inf=tmp.log
extract name="Ianodel" max(abs(i."anode"))
log off

log outf=tmp1.log
solve b1=1e-01 beam=1 lambda=0.1 wstep=0.025 wfinal=2.1
extract init inf=tmp1.log
extract name="EQE" curve(elect."optical wavelength (beam #1)," \
(-i."anode"-$Ianodel)/(elect."source photo current (beam #1)")) outf="part1.dat"

tonyplot part1.dat
log off

```

THIS PAGE LEFT INTENTIONALLY BLANK

APPENDIX B. PYTHON SCRIPTS

A. PREPROCESSING SCRIPT TO GENERATE RUN FILES

```
# -*- coding: utf-8 -*-

#@author: Silvio, modified by Ray Kilway

import codecs      # Keeping the Silvaco file in the right format
import csv        # Read in the CSV

with open("val.csv," "r") as csvfile:

    Input_data = csv.reader(csvfile)                      # Save the CSV in a variable

    for row_index, row in enumerate (Input_data): # Looping the Input data
matrix by row and generating the row index

        lines = []
        with codecs.open("dimroth.in," "r",encoding='utf8') as f: # Open the
default Silvaco scriped

            lines = f.readlines() # Read the scriped line by line

            for index in range (3, 3 +len(row)):      # index the line range where to
change the parameter

                parameter, value = lines[index].split("=", 1) # split the line at the
"=" chr

                if (index & 1) == 1:# Selecting the doping level lines in the skript

                    lines[index] = parameter + "=" + " " + str(row[index - 3]) + "\n" # Build the new content

                else:

                    stuff = float(1E16) * float(row[index - 3])
                    stuff = "%.3g" % stuff
                    lines[index] = parameter + "=" + " " + stuff + "\n" # Linear
transformation of the doping levels

            for out in [422, 432, 443]:           # Exception handling

                if out == 443:

                    residual = lines[out].split(".") # split the line at the . chrs

                    lines[out] = residual[0] + "." + residual[1] + "." + residual[2] +
str(row_index + 1) + "." + residual[3].rstrip('\n') + "\n" # Build the new
content
```

```

else:

    residual = lines[out].split(".") # split the line at the . chr

    lines[out] = residual[0] + str(row_index + 1) + "." + residual[1].rstrip('\n') + "\n" # Build the new content

    with codecs.open("Dimroth_Input_lin_xform_stacked" + str(row_index + 1) + ".in","w",encoding='utf8') as file: # Open a new file for each design

        for line in lines:

            file.write(line) # Write the lines into the file

        file.close()

```

B. RUN SCRIPT TO EXECUTE SILVACO ATLAS RUNS

```

# -*- coding: utf-8 -*-
"""

@author: Silvio, modified by Ray Kilway
"""

import subprocess      # Required to call other programs
import time            # Required to get the system time

timetracker = []       # Time capturing vector

for filenumber in range(1,11,1):      # Run of the number of designs

    outputcmd = "C:\sedatools\exe\deckbuild.exe -run
Dimroth_Input_lin_xform_stacked" + str(filenumber) + ".in"      # Specifying
the design to run in Silvaco

    start = time.time()      # Capturing the start time

    subprocess.check_output(outputcmd,shell=True)      # Call Silvaco to run the
design

    timetracker.append(time.time() - start)      # Appending the runtime to
the time vector

```

C. POSTPROCESSING SCRIPT TO EXTRACT OUTPUT POWER

```
# -*- coding: utf-8 -*-
"""
@author: Silvio, modified by Ray Kilway
"""

import numpy as np      # Required to apply multiplication to complete
vector
import pandas as pd      # Required to read in CSV file
import os.path

maxpower = []      # Vector to preserve the maximum output power

for filenumber in range(1, 11, 1):

    if os.path.exists('dimroth' + str(filenumber) + '.dat'):

        arr = np.loadtxt('dimroth' + str(filenumber) + '.dat', delimiter=' ',
skiprows = 4)      # Read the output value file from Silvaco

        maxpower.append (max(np.multiply(arr[:, 0], arr[:, 1])))      # Compute the
max power output value

    else:

        maxpower.append (0)

df = pd.read_csv('val.csv', header=None)      # Read the input value CSV
file

for c in df.columns:

    if (c & 1) == 1:

        df[c] = df[c].apply( lambda x: (float(1E16) * x))  # Linear transformation
of doping levels

new_column = pd.DataFrame(maxpower) # Change vector into pandas data frame
column

df = df.merge(new_column, left_index = True, right_index = True) # Merge input
and output data
df.to_csv('Dimroth_sim_results_1024_runs_iter1.csv',header=False, index=False)
      # Write the combined data back to a CSV ready for analysis
```

THIS PAGE LEFT INTENTIONALLY BLANK

LIST OF REFERENCES

- [1] P. Michalopoulos, “A novel approach for the development and optimization of state-of-the-art photovoltaic devices using Silvaco,” M.S. thesis, Dept. of Elec. and Comp. Engr., Naval Postgraduate School, Monterey, CA, 2002.
- [2] A. D. Bates, “Novel optimization techniques for multi-junction solar cell design using Silvaco ATLAS,” M.S. thesis, Dept. of Elec. and Comp. Engr., Naval Postgraduate School, Monterey, CA, 2004.
- [3] M. H. Tsutagawa, “Triple junction InGaP/GaAs/Ge solar cell optimization using Silvaco ATLAS,” M.S. thesis, Dept. of Elec. and Comp. Engr., Naval Postgraduate School, Monterey, CA, 2008.
- [4] M. H. Tsutagawa, “Genetic algorithm metaheuristic methodology and Silvaco® ATLAS™ to produce maximum power and efficiency solar cell designs,” Ph.D. dissertation, Dept. of Elec. and Comp. Engr., Naval Postgraduate School, Monterey, CA, 2013.
- [5] J. D. Utsler, “Genetic algorithm based optimization of advanced solar cell designs modeled in Silvaco ATLAS™,” M.S. thesis, Dept. of Elec. and Comp. Engr., Naval Postgraduate School, Monterey, CA, 2006.
- [6] J. E. O’Connor, “Design and simulation of novel high-efficiency, back-contact solar cells,” Ph.D. dissertation, Dept. of Elec. and Comp. Engr., Naval Postgraduate School, Monterey, CA, 2017.
- [7] S. Püschel, “Optimization of an advanced multi-junction solar-cell design for space environments (AM0) using nearly orthogonal Latin hypercubes,” M.S. thesis, Dept. of Op. Research, Naval Postgraduate School, Monterey, CA, 2017.
- [8] F. Dimroth, C. Baur, M. Meusel, S. van Riesen, and A. W. Bett, “5-Junction III-V solar cells for space applications,” in *3rd World Conference on Photovoltaic Energy Conversion*, Osaka, Japan, 2003, vol. 1, pp. 616–621.
- [9] F. Dimroth, C. Baur, A. W. Bett, W. Kostler, M. Meusel and G. Strobl, “Thin 5-junction solar cells with improved radiation hardness,” in *4th World Conference on Photovoltaic Energy Conversion*, Waikoloa, HI, 2006, pp. 1777–1780.
- [10] B. G. Streetman, S. K. Banerjee, *Solid State Electronic Devices*, 6th ed., Upper Saddle River, NJ: Pearson Prentice Hall, 2006.
- [11] S. O. Kasap, *Principles of Electronic Materials and Devices*, 3rd ed., New York, NY: McGraw-Hill, 2006.

- [12] S. M. Sze and K. K. Ng, *Physics of Semiconductor Devices*, 3rd ed., Hoboken, NJ: John Wiley & Sons, Inc., 2007.
- [13] R. Williams, “Becquerel photovoltaic effect in binary compounds,” *The Journal of Chemical Physics*, vol. 32, no. 5, pp. 1505–1514, May 1960.
- [14] A. B. Arons and M. B. Peppard, “Einstein’s proposal of the photon concept – a translation of the *Annalen der Physik* paper of 1905,” *American Journal of Physics*, vol. 33, no. 5, pp. 367–374, May 1965.
- [15] D. M. Chapin, C. S. Fuller, and G. L. Pearson, “A new silicon *p-n* junction photocell for converting solar radiation into electrical power,” *Journal of Applied Physics*, vol. 25, pp. 676–677, 1954.
- [16] W. Shockley and H. J. Queisser, “Detailed balance limit of efficiency of *p-n* junction solar cells,” *Journal of Applied Physics*, vol. 32, pp. 510–519, Mar. 1961.
- [17] F. Dimroth, T. N. D. Tibbits, M. Niemeyer, F. Predan, P. Beutel, C. Karcher, E. Oliva, G. Siefer, D. Lackner, P. Fuß-Kailuweit, A. W. Bett, R. Krause, C. Drazek, E. Guiot, J. Wasselin, A. Tauzin, and T. Signamarcheix, “Four-junction wafer-bonded concentrator solar cells,” *IEEE Journal of Photovoltaics*, vol. 6, no. 1, pp. 343–349, Jan. 2016.
- [18] P. T. Chiu, D.C. Law, R. L. Woo, S. B. Singer, D. Bhusari, W. D. Hong, A. Zakaria, J. Boisvert, S. Mesropian, R. R. King, and N. H. Karam, “35.8% space and 38.8% terrestrial 5J direct bonded cells,” in *40th IEEE Photovoltaic Specialist Conference*, Denver, CO, pp. 0011–0013, Jun. 2014.
- [19] K.F. Man, K.S. Tang, and S. Kwong, “Genetic algorithms: concepts and applications,” *IEEE Transactions on Industrial Electronics*, vol. 43, no. 5, pp. 519–534, Oct. 1996.
- [20] A. D. MacCalman, H. Vieira, and T. Lucas, “Second-order nearly orthogonal Latin hypercubes for exploring stochastic simulations,” *Journal of Simulation*, vol. 11, no. 2, pp. 137–150, May 2017.
- [21] A. D. MacCalman, “Flexible space-filling designs for complex system simulations,” Ph.D. dissertation, Dept. of Comp. Sci., Naval Postgraduate School, Monterey, CA, 2013.
- [22] *Atlas User’s Manual—Device Simulation Software*, Silvaco, Inc., Santa Clara, CA, 2016.
- [23] I. Vurgaftman, J. R. Meyer, L. R. Ram-Mohan, “Band parameters for III–V compound semiconductors and their alloys,” *Journal of Applied Physics*, vol. 89, no. 11, pp. 5815–5875, Jun. 2001.

- [24] A. V. Ivanov, V. D. Kurnosov, K. V. Kurnosov, A. A. Marmalyuk, V. I. Romantsevich, Yu. L. Ryaboshtan, and R. V. Chernov, “Refractive indices of solid AlGaInAs solutions,” *Quantum Electronics*, vol. 37, no. 6, pp. 545–548, 2007.
- [25] D. E. Aspnes, S. M. Kelso, R. A. Logan, and R. Bhat, “Optical properties of $\text{Al}_x\text{Ga}_{1-x}\text{As}$,” *Journal of Applied Physics*, vol. 60, pp. 754–767, Jul. 1986.
- [26] M. E. Levinshtein, S. L. Rumyantsev, and M. Shur, *Handbook Series on Semiconductor Parameters*, vol. 2, Singapore: World Scientific, 1999.
- [27] P. C. Mogensen, S. A. Hall, P. M. Smowton, U. Bangert, P. Blood, and P. Dawson, “The effect of high compressive strain on the operation of AlGaInP quantum-well lasers,” *IEEE Journal of Quantum Electronics*, vol. 34, no. 9, pp. 1652–1659, Sep. 1998.
- [28] O. Thériault, “Analysis of the external quantum efficiency of quantum dot-enhanced multijunction solar cells,” Ph.D. dissertation, Dept. of Phys., University of Ottawa, Canada, 2014.
- [29] H. Vieira, “NOB_Mixed_512DP,” Excel spreadsheet, 2012. [Online]. Available: <http://my.nps.edu/web/seed/software-downloads>

THIS PAGE INTENTIONALLY LEFT BLANK

INITIAL DISTRIBUTION LIST

1. Defense Technical Information Center
Ft. Belvoir, Virginia
2. Dudley Knox Library
Naval Postgraduate School
Monterey, California